Aerosol-meteorology feedback diminishes the trans-boundary transport of black carbon into the Tibetan Plateau

Yuling Hu[a], Shichang Kang[b, c, *], Haipeng Yu[a], Junhua Yang[b], Mukesh Rai[b], Xiufeng Yin[b], Xintong Chen[b], Pengfei Chen[b]

[a]Key Laboratory of Land Surface Process and Climate Change in Cold and Arid Regions, Northwest Institute of Eco-Environment and Resources, Chinese Academy of Sciences, Lanzhou 730000, China

[b]State Key Laboratory of Cryospheric Science, Northwest Institute of Eco-Environment and Resources, Chinese Academy of Sciences, Lanzhou 730000, China

[c]University of Chinese Academy of Sciences, Beijing 100049, China

Correspondence to: Shichang Kang (shichang.kang@lzb.ac.cn)

Abstract

Black carbon (BC) exerts potential effect on climate, especially in the Tibetan Plateau (TP), where the cryosphere and environment are very sensitive to climate change. The TP saw a record-breaking aerosol pollution event during the period from April 20 to May 10, 2016. This paper investigated the meteorological causes of the severe aerosol pollution event, the trans-boundary transport flux of BC, and the aerosol-meteorology feedback and its effect on the trans-boundary transport flux of BC during this severe aerosol pollution event via using observational and reanalysis datasets and simulation from the coupled meteorology and aerosol/chemistry model (WRF-Chem). By analyzing weather maps derived from the reanalysis dataset, it is found that the plateau

vortex and southerly winds were key factors that contributed to the severe aerosol pollution event. Subsequently, with the good performance of WRF-Chem model on the spatiotemporal characteristics of meteorological conditions and aerosols, the trans-boundary transport flux of BC during the pollution event was investigated. The results show that the vertically integrated cross-Himalayan transport flux of BC decreases from west to east, with the largest transport flux of 20.8 mg m^{-2} s^{-1} occurring at the deepest mountain valley in southwestern TP. Results from simulations with and without aerosol-meteorology feedback show that aerosols induce significant changes in meteorological conditions in the southern TP and the Indo-Gangetic Plain (IGP), with the atmospheric stratification being more stable and the planetary boundary layer height decreasing in both regions, and 10-m wind speed increasing in the southern TP but decreasing in the IGP. Changes in meteorological conditions in turn lead to a decrease in surface BC concentration with values up to 0.16 μg/m^3 (50%) in the southern TP and an increase of surface BC concentration with values up to 2.2 μg/m^3 (75%) in the IGP. In addition, it is found that the aerosol-meteorology feedback decreases the vertically integrated transboundary transport flux of BC from the central and western Himalayas towards the TP. This study not only provides crucial policy implications for mitigating glacier melt caused by aerosols over the TP but also is of great significance to the ecological environment protection for the TP.

Keywords: Tibetan Plateau; Black carbon; Transport flux; Aerosol-meteorology feedback; WRF-Chem

1 Introduction

Known as “the Third Pole”, the Tibetan Plateau (TP) plays a significant role in driving climate change in the Northern Hemisphere and even the globe through thermal and dynamical forcing (Wu et al., 2007;Lau et al., 2006). What’s more, with the most concentrated glacier and snow cover outside of the polar regions, the TP supplies a substantial portion of the water demand for almost 2 billion people (Yao et al., 2022). However, numerous studies from recent years have reported that the TP experienced significant and rapid climate warming during the last few decades (Kang et al., 2010;You et al., 2016;You et al., 2021). As a result of this intensive warming, glaciers over the TP have undergone unprecedented widespread losses and accelerated retreats (Kang et al., 2010;Yao et al., 2007). Besides high levels of greenhouse gases (Duan et al., 2006), other factors like atmospheric heating and snow albedo reduction due to absorbing aerosols also contribute a large portion to this climate warming and glacier retreat (Xu et al., 2009;Zhang et al., 2021;Kang et al., 2019b). However, with an average elevation exceeding 4 km, the TP is relatively undisturbed by human activities and is one of the most pristine regions on the earth. Hence, aerosols over the TP are mainly sourced from its surrounding regions (Kang et al., 2019b). Particularly, with nearly half of the world’s population and heavy industry, South and East Asia adjacent to the TP are the world’s hotspots for aerosol pollution (Lelieveld et al., 2016). Driven by atmospheric circulation, aerosols from South and East Asia can transport to the TP, and then exert a striking effect on the hydrological cycle and climate (Wu et al., 2008;Ramanathan et al., 2005;Liu et al., 2014). Previous studies indicated that aerosols

66 over the TP are primarily transported via typical long-distance trans-boundary transport
67 events (Kang et al., 2019a). It is therefore paramount to excavate the meteorological
68 causes of the severe aerosol pollution event as well as the trans-boundary transport flux
69 of aerosols during the severe aerosol pollution event.

70 Black carbon (BC) exerts a substantial impact on climate through several
71 mechanisms, including heating the atmosphere by absorbing shortwave and longwave
72 radiation, darkening the surface of snow and ice and accelerating the melt of the
73 cryosphere, and modifying the optical and microphysical properties of clouds (Kang et
74 al., 2019b;Ramanathan and Carmichael, 2008;Flanner et al., 2007;Skiles et al., 2018).
75 Estimation from the literature shows that BC is the second most important type of
76 human forcing after carbon dioxide, with a global climate forcing of 1.2 W m^{-2}
77 (Ramanathan and Carmichael, 2008;Chung et al., 2005). Moreover, the radiative
78 forcing of BC in snow and ice is approximately twice as high as that of carbon dioxide
79 and other types of anthropogenic forcing (Flanner et al., 2007;Qian et al., 2011;Hansen
80 and Nazarenko, 2004). Particularly, as a sensitive area to global climate change, the TP
81 has experienced an increase in BC content in recent years (Xu et al., 2009). There is no
82 doubt that BC plays a substantial role in the climate and environmental change over the
83 TP. However, previous studies primarily focused on the origin of BC and its climatic
84 effect over the TP on annual and seasonal timescales (Yang et al., 2018;Hu et al.,
85 2022b;Rai et al., 2022). With respect to the trans-boundary transport flux of BC towards
86 the TP during the severe aerosol pollution event on the synoptic scale, there is still a
87 blank, which should be studied urgently.

Severe aerosol pollution events are usually accompanied by complex aerosol-meteorology feedback. Moreover, numerous studies have revealed that the aerosol-meteorology feedback has a substantial effect on surface aerosol concentration (Wu et al., 2019;Zhang et al., 2018b;Zhao et al., 2017;Hong et al., 2020;Chen et al., 2019a;Gao et al., 2016). For instance, some studies analyzed the aerosol-meteorology feedback and its effect on surface $PM_{2.5}$ concentration during heavy aerosol pollution events in winter in northern China, and found that positive aerosol-meteorology feedback can increase the surface $PM_{2.5}$ concentration (Li et al., 2020;Qiu et al., 2017;Wu et al., 2019). Nonetheless, other studies suggested that the aerosol-meteorology feedback can reduce the surface $PM_{2.5}$ concentration in Beijing (Zheng et al., 2015;Gao et al., 2016). Based on in-situ observational data, Zhong et al. (2018) analyzed the aerosol-meteorology feedback during several air pollution events in Beijing and concluded that 70% of the increase in surface $PM_{2.5}$ concentration in the cumulative outbreak stage of haze could be attributed to the aerosol-meteorology feedback. The above-mentioned studies mainly focused on the economically developed central and eastern China regions. However, the TP has a very high altitude and complex topography along with a tough environment and scarce in-situ observational data. Systematic and comprehensive studies on aerosol-meteorology feedback in this region are still lacking and need urgent investigation. As studies related to the aerosol-meteorology feedback involve sensitivity tests, numerical simulation is the best way to realize the relevant research. In addition, a study conducted by Huang et al. (2020) indicates that the aerosol-meteorology interaction and feedback enhanced the trans-boundary transport of

pollutants between the North China Plain and the Yangzi River Delta regions and thus exacerbated the haze levels in these two regions simultaneously. For the Third Pole region, what effect the aerosol-meteorology feedback has on the trans-boundary transport flux of BC remains unclear, which worth an in-depth study. Therefore, in this study, we attempt to investigate the meteorological causes of the severe aerosol pollution event, the trans-boundary transport flux of BC, the aerosol-meteorology feedback and its effect on the trans-boundary transport flux of BC during the severe aerosol pollution event using observational and reanalysis datasets, and numerical simulation with the advanced regional climate-chemistry model, the Weather Research and Forecasting with Chemistry (WRF-Chem). This study not only provides crucial policy implications for mitigating glacier melt caused by aerosols over the TP, but also is of great significance to the ecological environment protection for the TP.

The structure of this paper is organized as follows. Following the introduction, data, definition of an aerosol pollution event, and WRF-Chem model configuration and experimental design are described in Section 2. In section 3, the meteorological causes of the severe aerosol pollution event, the trans-boundary transport flux of BC, the aerosol-meteorology feedback and its effect on the trans-boundary transport flux of BC during the severe aerosol pollution event are investigated. Section 4 presents the main conclusions.

2. Data, Definition of a severe aerosol pollution event, WRF-Chem model configuration, Emissions, and Experimental details

2.1 Data

2.1.1 ERA-Interim

To explore the meteorological causes of the severe aerosol pollution event, the geopotential height, air temperature (T), and wind fields at 500 hPa with a horizontal resolution of 0.05°×0.05° during the period from April 20 to May 10, 2016 are from the European Center for Medium-Range Weather Forecasts interim reanalysis (ERA-Interim). To evaluate the model performance on meteorology, 2-m air temperature (T2), 2-m dew point temperature, 10-m wind speed (U10), and wind fields at 500 hPa with a horizontal resolution of 0.05°×0.05° are also obtained from ERA-Interim. It should be noted that 2-m relative humidity (RH2) used to validate the model performance is calculated by 2-m dew point temperature and T2.

2.1.2 AERONET

The identification of aerosol pollution events on the TP is based on quality-assured data from the Aerosol Robotic Network (AERONET), which was established by the U.S. National Aeronautics and Space Administration (NASA) (Holben et al., 1998) and is used to retrieve aerosol properties via sun photometers (Dubovik and King, 2000). AERONET data, including instantaneous data and daily average by calculating the diurnal average of the instantaneous values (Holben et al., 1998), are available at three levels: level 1.0 (unscreened), level 1.5 (cloud-screened), and level 2.0 (cloud-screened

and quality assured data) (Smirnov et al., 2009). In this paper, the aerosol optical depth (AOD) and fine-mode AOD at a standard wavelength of 500 nm used to define the aerosol pollution event are based on the Spectral Deconvolution Algorithm (SDA) version 3, level 2.0 (O'Neill et al., 2003;O'Neill et al., 2008). In addition, this kind of AOD data was also used to verify the model performance on the temporal variation of AOD at different sites over the study area.

2.1.3 MODIS

The Moderate Resolution Imaging Spectroradiometer (MODIS) instrument aboard the Terra and Aqua satellites is designed with 36 spectral bands ranging from 0.4 to 15 μm and a high spatial resolution for retrieving reliable and extensive information about solar radiation, atmosphere, ocean, cryosphere, and land. The enhanced Deep Blue aerosol retrieval algorithm has substantially improved the collection of 6 aerosol products over the entire land region, especially in deserts and urban regions (Hsu et al., 2013). Herein, to verify the model performance on the spatial distribution of AOD, the AODs based on the Deep Blue algorithm at 550 nm with a horizontal resolution of 1°×1° and a daily temporal resolution from MODIS/Aqua Level-3 collection 6 products during the period from April 20 to May 10, 2016 are used. It should be noted that MODIS onboard the Aqua satellite passes over the equator at 13:30 local time.

2.1.4 MERRA-2

The second Modern-Era Retrospective analysis for Research and Applications

(MERRA-2), which is introduced to replace the original MERRA reanalysis because of the advances in the Goddard Earth Observing System Model, Version 5 (GEOS-5) data assimilation system, is a NASA atmospheric reanalysis, beginning in 1980 (Gelaro et al., 2017). MERRA-2 is the first long-term global reanalysis to assimilate space-based observations of aerosols, including assimilation of AOD retrieved from the Advanced Very High-Resolution Radiometer instrument over the oceans (Heidinger et al., 2014), the MODIS (Levy et al., 2010), non-bias-corrected AOD retrieved from the Multiangle Imaging SpectroRadiometer (Kahn et al., 2005) over bright surfaces, and ground-based AERONET observations (Holben et al., 1998). This dataset includes all the processes of aerosol transport, deposition, microphysics, and radiative forcing and has considerable skill in showing numerous observable aerosol properties (Gelaro et al., 2017;Randles et al., 2017), including dust, sulfate, organic carbon, BC, and sea salt aerosols (Chin et al., 2002;Colarco et al., 2010). As the first long-term aerosol reanalysis dataset, MERRA-2 has been adequately evaluated in previous studies (Buchard et al., 2017;Che et al., 2019;Sun et al., 2019). In this paper, the hourly surface BC concentration (kg/m^3), which has a spatial resolution of a longitude-by-latitude grid of approximately 0.625°×0.5°, is used to validate the model performance on BC. In addition, AOD from MERRA-2 combined with that from MODIS are used to validate the model performance on chemistry.

2.2 Definition of a severe aerosol pollution event

The two main reference sites used in this study are Nam Co Monitoring and Research Station for Multisphere Interactions (Nam Co), situated in inland TP

193 (30.77 °N, 90.96 °E, 4730 m a.s.l.), and Qomolangma Station for Atmospheric and
194 Environmental Observation and Research (QOMS, 28.36 °N, 86.95 °E, 4276 m a.s.l.),
195 located on the northern slope of Mt. Everest in the central Himalayas. The Nam Co and
196 QOMS stations joined the AERONET network in 2006 and 2009, respectively, and are
197 continuously functioning up to date. Both stations are background stations with fewer
198 human activities and can be regarded as representative sites for the inland of the TP and
199 the southern TP, respectively (Pokharel et al., 2019). Figure S1 in the supporting
200 information (SI) shows the daily mean of AOD at a standard wavelength of 500 nm
201 lying above the 95th percentile at Nam Co and QOMS stations since 2006 and 2009,
202 respectively. As can be seen, the observed most severe aerosol pollution event ever
203 recorded in the remote TP occurred during the period from April 27 to May 4, 2016,
204 persisting for at least eight days simultaneously at Nam Co and QOMS sites. Figure 1
205 presents the temporal variation in daily mean AOD and fine-mode AOD at 500 nm for
206 both stations during the period from April 20 to May 10, 2016. Notably, the changes in
207 daily mean AOD and fine-mode AOD are synchronized and the value of daily mean
208 fine-mode AOD is very close to that of daily mean AOD, indicating that the fine
209 particulate matter dominated this severe aerosol pollution event. Meanwhile, it is also
210 acquired from Figure 1 that the most polluted period during this pollution event is from
211 April 27 to May 4. Specifically, at Nam Co station, the observed highest daily mean
212 AOD and fine-mode AOD with values of 0.65 and 0.64 appeared on April 29, 2016;
213 while at QOMS station, the measured highest daily mean AOD and fine-mode AOD
214 with values of 0.42 and 0.39 occurred on May 1, 2016. According to the previous study,

the baseline values of AOD at Nam Co and QOMS are 0.029 and 0.027, respectively (Pokharel et al., 2019). Thus, the observed highest AOD at Nam Co and QOMS stations during this severe aerosol pollution event is at least one order of magnitude than that of baseline.

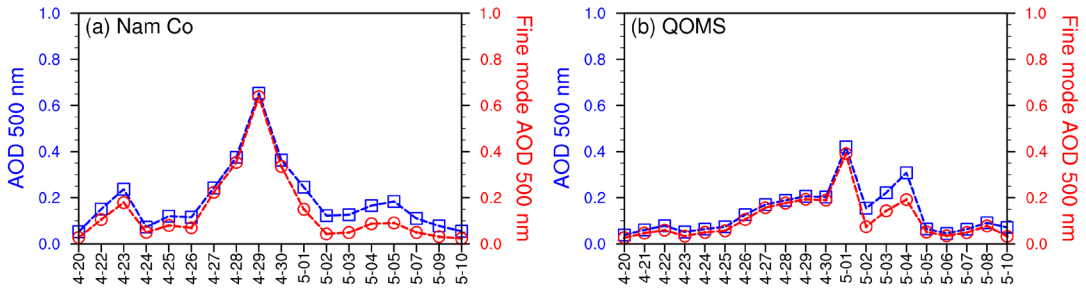

Figure 1. Time series of daily mean AOD (blue) and fine-mode AOD (red) at 500 nm at Nam Co (a) and QOMS (b) stations during the period from April 20 to May 10, 2016.

2.3 WRF-Chem model configuration, Emissions, and Experimental design

The WRF-Chem model is a fully coupled regional dynamical/chemical transport model that considers gas-phase chemistry, photolysis, and aerosol mechanism (Grell et al., 2005). The model can simulate the emission, transport, mixing, chemical reactions, and deposition of trace gases and aerosol simultaneously with the meteorological fields. It has been successfully applied in air pollution studies over the TP and adjacent regions (Yang et al., 2018;Chen et al., 2018;Hu et al., 2022b). The version used in this study is based on v3.9.1. As shown in Figure 2, the simulation domain is centered at 31°N, 87.5 °E, covering the whole TP and its surroundings. Numerous previous modeling studies on aerosol-meteorology feedback were carried out using a model domain with a horizontal resolution of 20 km or even coarser (Hu et al., 2022a;Zhang et al., 2018a;Li

et al., 2022;Bharali et al., 2019;Gao et al., 2015;Huang et al., 2020). Considering the topography over the TP is very complex, model simulations in this study are conducted at a 15-km horizontal resolution using a Lambert conformal mapping with 259 (west-east) × 179 (north-south) grid cells. There are 30 vertical sigma levels for all grids, extending from the surface to 50 hPa. The key physical parameterization options used in this study include the Noah land surface model (Ek et al., 2003;Chen et al., 2010) and the Monin-Obukhov scheme for the surface layer physical processes (Srivastava and Sharan, 2017), the double-moment Morrison microphysical parameterization (Morrison et al., 2009) with the Grell-Freitas (GF) cumulus scheme (Grell and Freitas, 2014), the Mellor-Yamada-Janjic (MYJ) planetary boundary layer scheme with local vertical mixing (Janjić, 1994), and the Rapid Radiative Transfer Model for General circulation models (RRTMG) coupled with the aerosol radiative effect for both longwave and shortwave radiation (Iacono et al., 2008). With respect to the chemical parameterization options, the Carbon-Bond Mechanism version Z (CBMZ) gas-phase chemistry mechanism (Zaveri and Peters, 1999) combined with the Model for Simulating Aerosol Interactions and Chemistry (MOSAIC) aerosol module (Zaveri et al., 2008) was chosen for aerosol simulation. The MOSAIC aerosol scheme uses an approach of segmentation to represent aerosol size distribution with four or eight discrete size bins (Fast et al., 2006). In this paper, the aerosol size is divided into four bins. Aerosol species simulated by the MOSAIC scheme include sulfate, methanesulfonate, nitrate, chloride, carbonate, ammonium, sodium, calcium, BC, primary organic mass, liquid water, and other inorganic mass.

256 The initial and boundary conditions for meteorological fields are obtained from
257 the National Centers for Environmental Prediction (NCEP) Final Analysis (FNL) data
258 with a 1° × 1° spatial resolution and a 6-h temporal resolution
259 (https://rda.ucar.edu/datasets/ds083.2/). Anthropogenic emissions, such as CO, VOCs,
260 NOx, NH_3, BC, OC, SO_2, $PM_{2.5}$, and PM_{10}, are taken from the Emission Database for
261 Global Atmospheric Research (EDGAR)-Hemispheric Transport Air Pollution version
262 2 (HTAPv2) emission inventory (https://edgar.jrc.ec.europa.eu/dataset_htap_v2) for the
263 year 2010. Detailed information on the HTAP inventory can be found in Janssens-
264 Maenhout et al. (2015). The biogenic emissions are based on the Model of Emissions
265 of Gases and Aerosols from Nature (MEGAN) (Guenther et al., 2006;Guenther et al.,
266 2012), and the biomass burning emissions were calculated with the high-resolution fire
267 emissions based on the Fire INventory from NCAR (FINN) (Wiedinmyer et al., 2011) .
268 In addition, the mozbc utility and the Community Atmosphere Model with
269 Chemistry (CAM-Chem) (Buchholz et al., 2019) dataset are used to create improved
270 chemical initial and boundary conditions. The simulation is conducted from April 10,
271 2016 to May 10, 2016, and the first ten days are used for model spin-up. The results
272 from April 20, 2016 to May 10, 2016 are used for the analysis.
273 There are two experiments involved in this study, one is the control experiment
274 (CONT) and the other is the sensitive experiment (SEN). In the CONT, the simulation
275 is conducted using the WRF-Chem model with aerosol-meteorology feedback turned
276 on. The SEN is exactly the same as CONT except that the feedback between aerosol
277 and meteorology is turned off. The difference between CONT and SEN is considered

as the effect induced by aerosol-meteorology feedback.

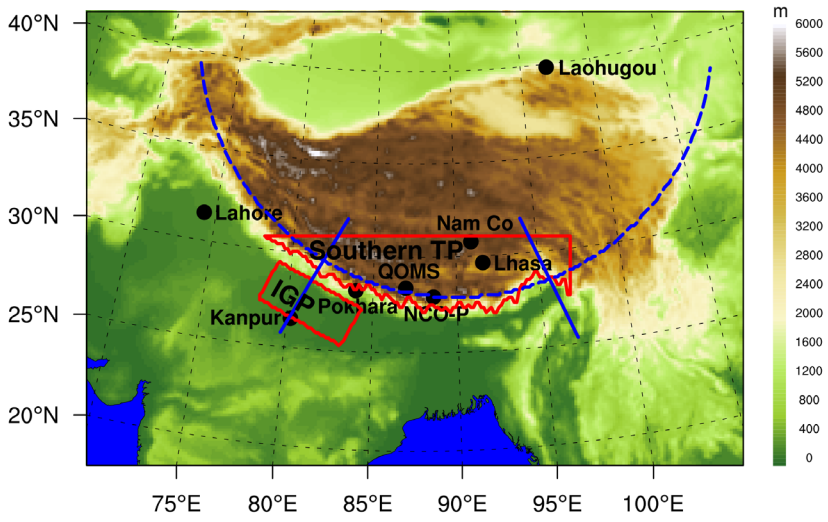

Figure 2. WRF-Chem model domain and terrain (shading; m). Black solid dots denote stations used to verify model performance on meteorological conditions and aerosols. The solid red lines and its inner area denote the southern TP and Indo-Gangetic Plain. The blue dashed line and two solid lines represent the cross sections for analysis in the following.

3 Results and discussion

3.1 Meteorological causes of the severe aerosol pollution event

Excessive emissions and adverse meteorological conditions are the two most important factors influencing air quality (Wang et al., 2019;Chen et al., 2019b;Liu et al., 2017;Zhang et al., 2019). The TP, which has a small population density and a low degree of industrialization, is one of the most pristine regions on the earth. Moreover, as mentioned above, from April 27 to May 4, 2016, AOD at background stations of Nam Co and QOMS with fewer human activities is significantly higher than that of baseline with the highest value at least one order of magnitude than that of baseline.

Therefore, it can be inferred that aerosols over the TP during this severe aerosol pollution event are mainly sourced from adjacent regions by long-range transport, which is consistent with the results reported in a previous study (Kang et al., 2019b). Atmospheric circulation, as the main driving force of atmospheric aerosols, plays a substantial role in the long-range transport of aerosols. Therefore, with little change in emission source, analyzing the meteorological conditions during a severe pollution event is very crucial. Figure 3 shows weather maps at 500 hPa based on the ERA-Interim reanalysis dataset. It is found that, during 08:00–14:00 Beijing Time (hereafter BJT) on April 27, straight westerly airflow prevailed at 500 hPa over the TP (Figure 3a), which transported aerosols from northwestern South Asia to the TP. Subsequently, wind field shear occurred over the plateau at 20:00 on April 27 (Figure 3b), and plateau vortex generated at 02:00 on April 28 (Figure 3c), which is conducive to the accumulation of aerosols in the inland of the plateau. From 08:00 on April 28 to 08:00 on April 29, the plateau vortex stabilized over the TP, and the aerosol concentrations at Nam Co station continued increasing (figure not shown). At 14:00 on April 29, the plateau vortex disappeared (Figure 3d) and the aerosol concentrations peaked at Nam Co station. Meanwhile, a high-pressure system was located on the west side of the plateau accompanied by a trough on the foreside (Figure 3d). Thus, southwesterly airflow in front of the trough transported aerosols from northern South Asia to the southern TP (Figure 3e). As a result, the aerosol concentrations at QOMS station increased and peaked on May 1. At 14:00 on May 1, the high-pressure system moved eastward from the west side to the inland of the TP and northerly winds ahead of this

high-pressure system prevailed over the TP (Figure 3f), which wafted aerosols away from the TP and aerosol concentrations at QOMS station began to decrease.

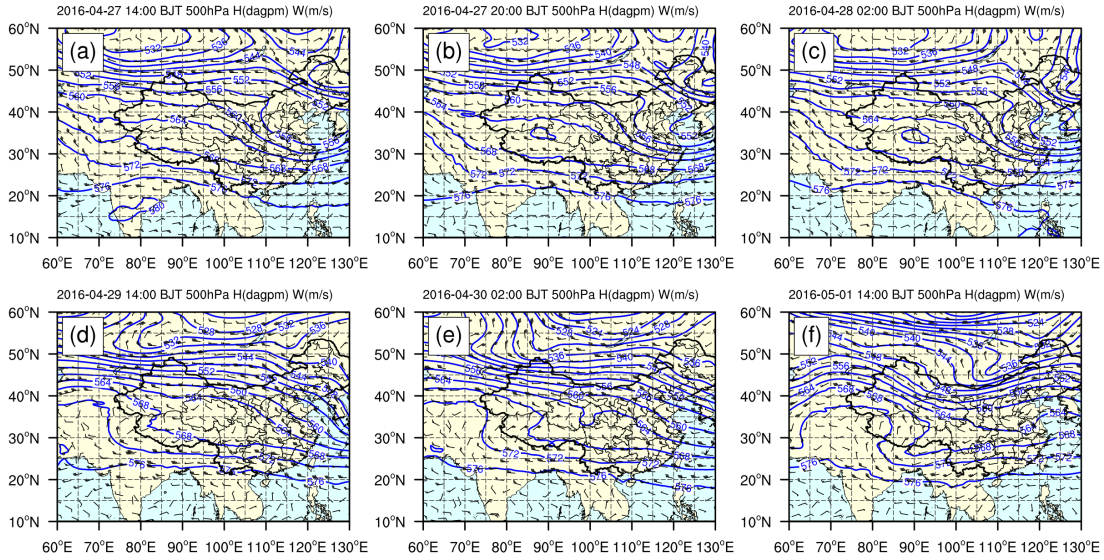

Figure 3. Weather maps at 500 hPa over the study area during the severe aerosol pollution event based on the ERA-Interim reanalysis dataset. The blue lines are isopleths of geopotential height (unit: dagpm). Wind speed (unit: m/s) and direction are denoted by wind barb.

3.2 Evaluating model performance on meteorology and chemistry

3.2.1 Validation of model performance on meteorology

Validating model performance on meteorology is critical for assuring accuracy in simulating aerosol concentrations. This is because meteorological conditions are closely associated with aerosol growth, transport, and deposition. Herein, to validate the model performance on meteorological conditions, the temporal variation in the simulated and reanalyzed T2, RH2, and U10 at Nam Co, QOMS, Kanpur, and Lahore stations are shown in Figure S2 in the SI. The model reasonably represents the correct

temporal trend of T2 at four stations although underestimations are detected at Nam Co and QOMS stations. The variation trend of RH2 from the simulation is in high consistent with that from reanalysis at Kanpur and Lahore stations. However, at Nam Co and QOMS stations, a relatively larger discrepancy is observed between simulation and reanalysis, which might be related to the high altitude and complex topography there. For U10, the simulated trend on average coincides with the observed trend at Nam Co, Kanpur, and Lahore stations. The corresponding statistics, including sample size (N), observed mean, simulated mean, mean bias (MB), normalized mean bias (NMB), root mean square error (RMSE), and correlation coefficient (R) between observation and simulation at different stations are shown in Table S1 in the SI. The calculations indicate that T2 is well simulated with MB of −4.25, −3.62, 0.03, and 0.07, and R of 0.69, 0.87, 0.94, and 0.96 at Nam Co, QOMS, Kanpur, and Lahore stations, respectively. RH2 and U10 are less well simulated, especially at Nam Co and QOMS stations, where the altitude is very high and the terrain is fairly complex. To be exact, RH2 with MB of 29.68 and −25.82 and R of 0.51 and 0.52 are obtained at Nam Co and QOMS stations, respectively. And U10 with MB of 0.91 and 5.66 and R of 0.30 and 0.55 are detected at two stations accordingly. However, at Kanpur and Lahore stations, RH2 and U10 from reanalysis and simulation are in high consistency, with MBs of −12.56 and 0.85, −13.00 and 0.96, Rs of 0.80 and 0.45, 0.78 and 0.22, respectively. As a whole, U10 is on average overestimated at four stations and has a greater range of about 3.43–8.56 m/s compared to reanalyzed values with a range of about 2.47–3.39 m/s. Hence, the simulations are biased at least in part since the model grid represents a

355 regional average at 15 × 15 km^2 in a domain of great topographic complexity, and the
356 values derived from reanalysis with a horizontal resolution of 0.05°×0.05° represent a
357 regional average of a relatively higher resolution. In addition, the accuracy of the
358 gridded observational data of ERA-interim is correlated with the restriction of the
359 observations assimilated into the reanalysis and with the different assimilation methods
360 (Chung et al., 2013). Overall, we conclude that the WRF-Chem model exhibits
361 acceptable performance in simulating temporal variations in meteorological elements.
362 The spatial distributions of T2, RH2, and wind field at 500 hPa from simulation
363 and reanalysis over the domain are presented in Figure S3 in the SI. Spatially, both
364 simulation and reanalysis show similar spatial patterns for each of the above-mentioned
365 meteorological fields. Exactly, surface air temperature with high values mainly appears
366 over regions surrounding the TP, especially obvious over South Asia where surface air
367 temperature exceeds 30 °C. Previous studies indicated that surface air temperature over
368 the Indian subcontinent is the highest during the pre-monsoon season because the
369 Himalayas block the frigid katabatic winds flowing down from Central Asia during this
370 period (Ji et al., 2011). In contrast, surface air temperature with low values mainly
371 occurs over the TP. Different from T2, RH2 with high values primarily appears over
372 the TP, the Bay of Bengal, and central and eastern China but with low values in the rest
373 area of the domain. Particularly, RH2 in the southeastern TP is apparently higher than
374 that of the inland of the TP, because the southeastern TP is in proximity to the moisture
375 sourced from the Bay of Bengal. Moreover, the reason why the spatial distribution of
376 T2 is antiphase with that of RH2 is that the decrease in T2 can lead to a decrease in the

saturation pressure of water vapor and an increase in RH2 at the surface (Gao et al., 2015). With respect to the 500 hPa wind field, both simulation and observation show that the westerly winds prevail over the entire region. Due to the high topography of the TP, such westerly winds are divided into two branches at appropriate 75 °E. One branch flow eastward, and the other branch is forced up by the high plateau and subsequently shifts to the northwesterly wind. Therefore, the WRF-Chem model also effectively simulates the spatial distributions of T2, RH2, and 500 hPa wind fields. Overall, this simulation configuration captures the meteorological fields well, which is critical to assure simulation accuracy of air pollutant concentrations.

3.2.2 Validation of model performance on AOD and BC

To validate the model performance on simulating spatiotemporal variations in aerosols, ground-based AOD from AERONET together with reanalyzed AOD from MERRA-2 is compared to simulated AOD first. Figure S4 shows the temporal variations in simulated and observed daily mean AOD at Nam Co, QOMS, and Pokhara stations for the period from April 20 to May 10, 2016. As a whole, the WRF-Chem model reasonably reproduces the temporal variations in AOD at each of the above stations, with a relatively larger bias at Nam Co and Pokhara stations and a smaller bias at QOMS station. The specific statistics for N, observed mean, simulated mean, MB, NMB, RMSE, and R between observed and simulated AOD at different stations are shown in Table S2 in the SI. As we note that one-third of AOD values at the selected stations in the MERRA-2 dataset during the study period is missing, the statistical description between the reanalyzed and simulated AOD is not presented. The results

399 from Table S2 indicate that MB with values of −0.13, −0.01, and −0.57, and R with
400 values of 0.58, 0.42, and 0.56 are obtained at Nam Co, QOMS, and Pokhara,
401 respectively. Moreover, AOD from observation is significantly correlated with that
402 from simulation at Nam Co and Pokhara stations, with the correlation coefficient
403 passing the 95% confidence level. In addition, we note that AOD from the simulation
404 is on average lower than that from observation, which may be due to the assumed
405 spherical aerosol particles in the model simulation. The optical properties of particles
406 are more sensitive to non-spherical morphology than primary spherical structure (China
407 et al., 2015;He et al., 2015). On the whole, the model effectively reproduces the
408 observed temporal variation in AOD.

409 Spatially, the spatial pattern of simulated AOD is in consistent with that from
410 either MODIS or MERRA-2 reanalysis dataset, suggesting a reliable performance of
411 WRF-Chem on simulating AOD. Specifically, AOD from simulation, MODIS, and
412 MERRA-2 shows distinct spatial distribution characteristics, with high values in
413 northern South Asia, the Bay of Bengal, Southeast Asia, and the Sichuan Basin and low
414 values over the TP (Figure S5). This is because northern South Asia, Southeast Asia,
415 and the Sichuan Basin are heavily industrialized and densely populated regions
416 compared to the TP (Bran and Srivastava, 2017). In the Taklimakan Desert, AOD
417 monitored by satellite is much higher than that obtained from simulation, which is likely
418 due to the uncertainty of the emission inventory. Taken together, the comparison
419 between simulation from WRF-Chem and observation from AERONET, MODIS, and
420 MERRA-2 shows that the WRF-Chem model captures the overall spatio-temporal

421 characteristics of AOD over the domain.

422 To verify the capability of this framework of WRF-Chem on simulating BC
423 concentration, we present the temporal variation in simulated and reanalyzed hourly
424 BC concentrations at Nam Co, QOMS, Lhasa, NCO-P, Laohugou, and Kanpur stations
425 during the period from April 20 to May 10, 2016, as shown in Figure 4. It is found that
426 the WRF-Chem model overall reproduces the temporal variation in reanalyzed BC
427 concentrations at different stations. The specific statistics for N, observed mean,
428 simulated mean, MB, NMB, RMSE, and R between the reanalyzed and simulated
429 hourly BC concentrations at different stations are shown in Table S2 in the SI. As can
430 be seen, MB with values of −0.07, 0.14, −0.02, −0.02, 0.02, and 0.72, and R with values
431 of 0.67, 0.43, 0.47, 0.50, 0.25, and 0.64 are obtained at Nam Co, QOMS, Lhasa, NCO-
432 P, Laohugou, and Kanpur stations, respectively. The reanalyzed and simulated hourly
433 BC concentrations are strongly correlated at each of the stations, with the correlation
434 coefficient exceeding the 99% confidence level. Besides the reanalyzed hourly BC
435 concentration, the in-situ BC observation is available at the QOMS station. The inter-
436 comparison among in-situ observed, simulated, and MERRA-2 reanalyzed daily mean
437 BC concentrations at the QOMS station was further conducted, as shown in Figure S6.
438 It is apparent that the temporal variation in simulated daily mean BC concentrations is
439 very close to that of observed daily mean BC concentrations. The correlation coefficient
440 between the simulated and observed daily mean BC concentrations is 0.867, passing
441 the 99% confidence level. Hence, the WRF-Chem model exhibits a better performance
442 in simulating BC concentrations.

Because the spatial distribution of BC concentration retrieved from CAM_Chem dataset is not reasonable (Figure S7a), the inter-comparison between WRF-Chem simulated and reanalyzed BC concentrations over the domain was performed to validate the model performance on the spatial distribution of BC concentrations. Figure S7b-c presents the spatial distribution of simulated and reanalyzed BC concentrations over the domain averaged for the period from from April 20 to May 10, 2016. It can be found that BC concentrations from both simulation and reanalysis display distinct spatial variability, with low concentrations over the TP and high concentrations over the north of South Asia, Southeast Asia, and the Sichuan Basin. As one of the most pristine regions on the earth, the TP has a small population density and a low degree of industrialization, resulting in low BC concentrations. Nonetheless, regions adjacent to the TP like north of South Asia, Southeast Asia, and the Sichuan Basin with low elevations have dense populations and developed industrialization (Li et al., 2016a;Qin and Xie, 2012;Li et al., 2016b), emitting large amounts of BC into the atmosphere and resulting in high BC concentrations. Therefore, the WRF-Chem model can capture the main temporal and spatial features of BC concentrations over the TP and adjacent regions.

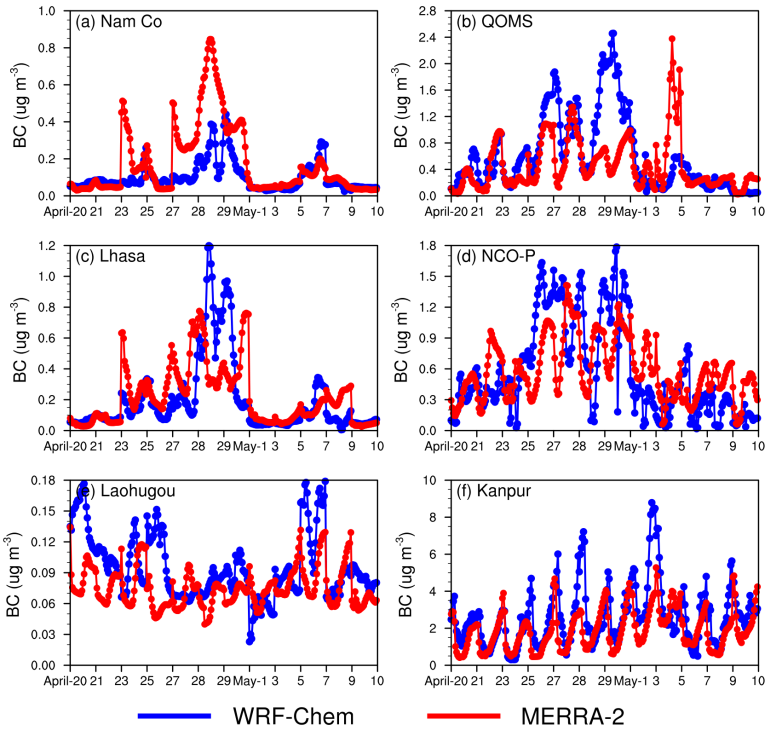

Figure 4. Temporal variations in simulated and reanalyzed hourly BC concentrations at Nam Co (a), QOMS (b), Lhasa (c), NCO-P (d), Laohugou (e), and Kanpur (f) stations for the period from April 20 to May 10, 2016.

3.3 Trans-boundary transport flux of BC

The foregoing analysis has validated the model framework used in this study and the results are basically satisfactory. BC, as the major component of light-absorbing particles, exerts a significant impact on climatic and cryospheric changes over the TP due to its strong light absorption and important effect on snow and ice albedo (Kang et al., 2010;Kang et al., 2019b;Yang et al., 2018). In this section, the trans-boundary transport flux of BC during this severe aerosol pollution event is investigated. According to a previous study, the BC transport flux can be calculated by projecting the wind field perpendicularly to the cross line and then multiplying the BC mass

concentration along the cross line (Zhang et al., 2020). More specifically, the BC transport flux is calculated as follows:

$$\mathrm{TF} = \mathrm{C} \cdot (u \cdot \sin\alpha + v \cdot \sin\beta), \quad (1)$$

where α is the angle between the east–west wind component and the cross line, β is the angle between the south–north wind component and the cross line, and C is the BC mass concentration at the grid along the cross line. The flux is estimated at each model level. Positive values represent the transport towards the TP, while negative values represent the transport away from the TP. Figure 5 presents the longitude-height cross section of BC transport flux along the cross line (shown as the blue dashed lines in Figure 2) from the simulation with aerosol-meteorology feedback at 15:00 and 03:00 BJT averaged for the period from April 27 to May 4 (the most polluted period) to represent daytime and nighttime transport, respectively. Notably, in the central and western Himalayas (to the west of ~94 °E), BC is imported into the TP during both day and night times, especially obvious at the height of below 7 km, although the transport flux during the nighttime is higher than that during the daytime. In the eastern Himalayas (from 94–98 °E), BC is imported into the TP during the day but exported slightly from the TP during the night. To the east of ~98 °E, BC is transported away from the TP during the day and night due to the prevailed westerly winds. Generally, the transport across the western Himalayas is controlled by the large-scale westerly, while the transport across the central and eastern Himalayas is primarily dominated by a local southerly (Zhang et al., 2020). Therefore, the difference in BC transport flux between the western and eastern Himalayas is attributed to the influence of a large-scale

496 westerly that is weak over the eastern Himalayas. The stronger diurnal variation of local
497 southerly (towards the TP in the daytime to away from the TP in the nighttime)
498 compared to that of a westerly near the surface leads to the large difference in diurnal
499 variation of the transport between the western and eastern Himalayas. In addition, the
500 largest BC transport flux along the cross line occurs at deeper mountain valley channels
501 (Figure 5). Zhang et al. (2020) investigated the impact of topography on BC transport
502 to the southern TP during the pre-monsoon season and found that the BC transport
503 across the Himalayas could overcome the majority of mountain ridges, but the valley
504 transport is more efficient, which is consistent with the results obtained in this study.
505 As the largest BC transport flux occurs at deeper mountain valleys, the two deepest
506 mountain valley channels along the cross line shown as the blue solid line in Figure 2
507 are selected to demonstrate the BC transport flux across mountain valleys during this
508 severe pollution event. The first valley (referred to as valley-1 hereon) is located in the
509 southwestern TP, while the second valley (referred to as valley-2 hereon) is located in
510 the southeastern TP. It is seen that, at valley-1, the overall positive values near the
511 surface indicate that BC is imported into the TP during the daytime and nighttime,
512 though the transport flux at night is much higher than that during the daytime (Figure
513 5). Averaged BC concentration and transport flux at 03:00 and 15:00 BJT during the
514 period from April 27 to May 4, 2016 across valley-1 from the simulation with aerosol-
515 meteorology feedback also shows that the BC transport flux is much higher during the
516 night than that during the daytime (Figure 6a–b). By checking the surface BC
517 concentration from simulation with aerosol-meteorology feedback, it is found that the

surface BC concentration at valley-1 during the night is much higher than that during the daytime (Table 1). Moreover, the vertically integrated BC concentration over the Himalayas is much higher in the nighttime than that in the daytime (Figure S8). With the help of the large westerly winds, BC then is transported to the TP, which further provides evidence for the higher BC transport flux during the night shown in Figure 6b. At valley-2, the near-surface positive flux values during the daytime and negative values during the night denote that BC is imported into the TP during the daytime but exported slightly from the TP at night (Figure 5). To analyze this distinct diurnal variation in BC transport flux, we present the latitude–height cross section of BC transport flux and its concentration at 03:00 and 15:00 BJT averaged for the period from April 27 to May 4, 2016 across valley-2 from the simulation with aerosol-meteorology feedback as shown in Figure 6c–d. Notably, the deeper PBLH and the strong turbulent mixing during the daytime over northern India allows BC to be mixed at a higher altitude (Figure 6c). Subsequently, the local southerlies boost the BC transporting across the eastern Himalayas towards the TP. Nevertheless, during the night, the meridional wind is dominated by a northerly over the eastern Himalayan region (Figure 6d), suggesting the cross-Himalayan transport is away from the TP.

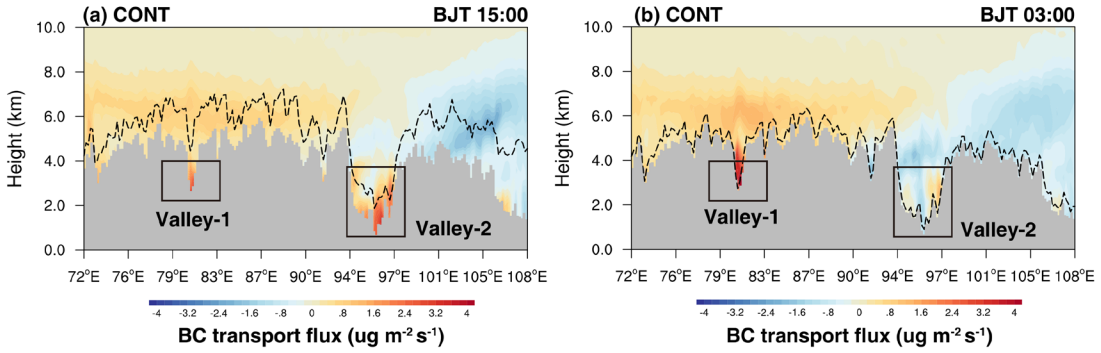

Figure 5. Longitude–height cross section of BC transport flux along the cross line

(shown as the blue dashed line in Figure 2) at 15:00 and 03:00 BJT averaged for the period from April 27 to May 4, 2016 from simulation with aerosol-meteorology feedback. The PBLH along the cross section is shown here as the black dashed line.

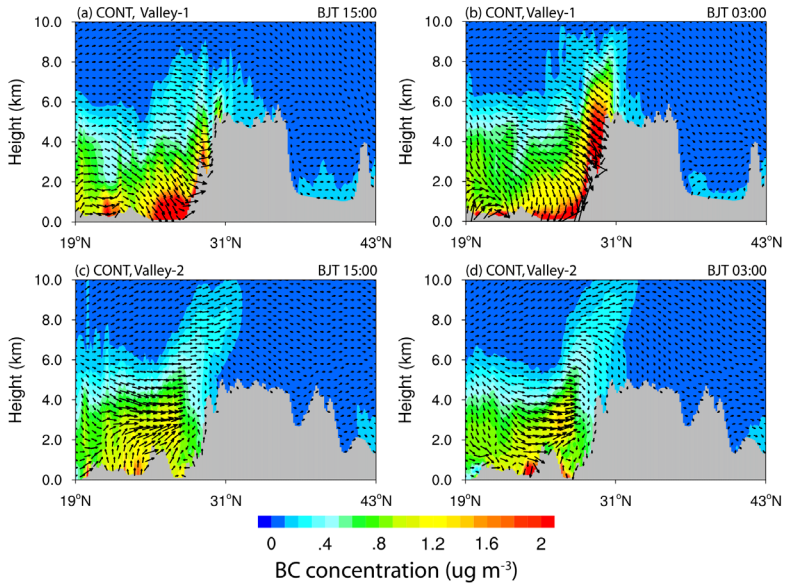

Figure 6. Latitude–height cross section of BC transport flux (vector) across the mountain (a, b) valley-1 and (c, d) valley-2 at 15:00 and 03:00 BJT averaged for the period from April 27 to May 4, 2016 from simulation with aerosol-meteorology feedback. Contour represents the BC concentration.

Table 1. Surface BC concentration at two typical mountain valley channels at 15:00 and 03:00 BJT averaged for the period from April 27 to May 4, 2016 from simulation with aerosol-meteorology feedback.

Near-surface BC concentration	15:00		03:00	
	Valley-1	Valley-2	Valley-1	Valley-2
CONT	1.27	0.75	2.55	0.46

To further demonstrate the overall inflow flux across the Himalayas, the vertically integrated BC mass flux along the longitudinal cross section as shown in Figure 5 from simulation with aerosol-meteorology feedback is shown in Figure 7. The total mass flux is calculated by integrating the right-hand term of Eq. (1) as follows:

$$ITF = \int_{z=z_{sfc}}^{z=z_{top}} \delta z \cdot C \cdot (\mu \cdot sin\alpha + v \cdot sin\beta)\,, \quad (2)$$

where δz is the thickness of each vertical model level. Similarly, positive flux values represent the transport towards the TP, while negative values represent the transport away from the TP. It has been found that the positive values primarily exist in the central and western Himalayas (to the west of 92 °E), while negative values mainly exist to the east of 92 °E (Figure 7). Furthermore, the vertically integrated transport flux of BC along the cross line is strongly correlated with the longitudinal degree of the cross line, with the correlation coefficient up to −0.89, passing the 99% confidence level. This indicates that the vertically integrated transport flux of BC along the cross line decreases from west to east. In particular, from 80 to 86 °E along the cross line, the correlation coefficient between the terrain height and the vertically integrated transport flux of BC is −0.87, exceeding the 99% confidence level, suggesting that the lower the valleys are, the higher the vertically integrated transport flux transported across the Himalayas can be. Particularly, the largest vertically integrated transport flux about 20.8 mg m^{-2} s^{-1}occurs at valley-1. However, to the eastern Himalayas (to the east of ~92 °E), the BC is overall exported away from the TP and the vertically integrated transport flux with the largest value near to zero occurs at valley-2.

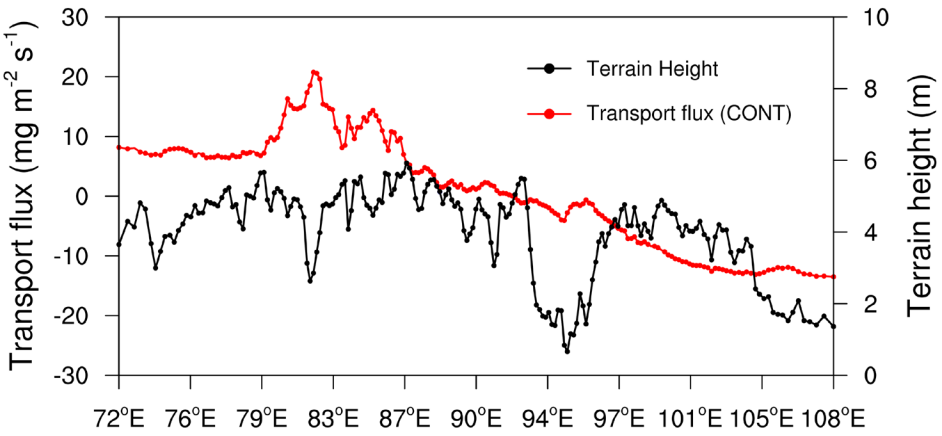

572

573 Figure 7. Longitudinal distribution of vertically integrated BC mass flux (red line) along
574 the cross section in Figure 2 from simulation with aerosol-meteorology feedback. The
575 black line represents the terrain height.

576

577 *3.4 Aerosol-meteorology feedback during the severe aerosol pollution event*

578 Generally, the severe aerosol pollution event is accompanied by complex feedback
579 between aerosol and meteorology. The analysis above confirms that BC in northern
580 South Asia can be transported to the TP via the cross-Himalayan transport during this
581 severe pollution event. Moreover, compared to the eastern Himalayas, the western
582 Himalayas contributes more BC to the TP and BC from the cross-Himalayan transport
583 mainly concentrated in the southern TP. Therefore, in this section, the feedback
584 between aerosol and meteorology over the western Indo-Gangetic Plain (referred to
585 IGP hereon) and southern TP during this severe pollution event is analyzed.

586 To illustrate the aerosol radiative forcing (ARF) and its impacts on T2, RH2,
587 surface energy, atmospheric stability, wind, and PBLH over the southern TP and IGP
588 regions, the time series of aerosol-induced daily and diurnal changes in meteorological
589 variables (T2, RH2) and surface energy budget (latent heat (LH), sensible heat (SH),

shortwave (SW) radiation, longwave (LW) radiation, and net energy flux (LH+LW+SH+SW)) averaged for the southern TP and IGP regions, which is calculated by subtracting the model results of SEN from those of CONT, is shown in Figure 8. It should be noted that the diurnal change is calculated for the most polluted period from April 27 to May 4. As can be seen, the daily variation of aerosol-induced area-averaged surface air temperature ranged from −0.1 to 0.1 °C in the southern TP, with a discernable decrease of 0.1 °C appearing on May 2, May 4, and May 6–7 (Figure 8a), and from −1.7 to 1.2 °C in the IGP (Figure 8c) during the period from April 20 to May 10. During the most polluted period from April 27 to May 4, the aerosol-induced surface air temperature ranged from −0.1 to 0.1 °C in the southern TP (Figure 8a), with a decrease of 0.1 °C on May 2 and May 4, and decreased by 0.5–1.7 °C in the IGP (Figure 8c). The daily variation of aerosol-induced area-averaged RH2 displayed a slight change with values ranging from −1.6% to 2.3% over the southern TP (Figure 8a) and exhibited a greater range of about −10.9%–13.7% in the IGP (Figure 8c) during the period from April 20 to May 10. From April 27 to May 4 with high aerosol concentrations, area-averaged RH2 increased by 0–2.3% and by 0.8%–13.7% in the southern TP and IGP, respectively (Figure 8a, c). For the diurnal change depicted in Figure 8b and Figure 8d, during 09:00–20:00 BJT in the daytime, the aerosol-induced area-averaged surface air temperature had a range of about −0.1–0.1 °C in the southern TP and decreased by 0.9–2.3 °C in the IGP. At night, surface air temperature increased by 0.1°C during 00:00–05:00 BJT in the southern TP (Figure 8b), and decreased by 0–1.0 °C during 21:00–08:00 BJT in the IGP (Figure 8d). The corresponding diurnal

612 change in aerosol-induced RH2 indicated that the aerosol-induced RH2 decreased by
613 0.1%–0.4% during 14:00–17:00 BJT in the southern TP but increased during the rest
614 time of the day, with the maximum increase of 1.3% occurring during 09:00–10:00 BJT
615 (Figure 8b). In the IGP, the aerosol-induced RH2 increased by 3.3%–7.1% during
616 09:00–20:00 BJT in the daytime and increased by 2.6%–4.5% during 21:00–08:00 in
617 the nighttime (Figure 8d). Therefore, the aerosol-induced changes in T2 and RH2
618 primarily occur in the daytime.

619 Generally, surface energy with positive values indicates more energy flux toward
620 the surface, and vice versa. Figure 8e–h shows the aerosol-induced surface energy
621 changes over the southern TP and IGP, it is found that the SW radiation flux at the
622 surface decreased by 0–13.7 Wm^{-2} in the southern TP (Figure 8e) and by 44.5–75.3
623 Wm^{-2} in the IGP (Figure 8g) during the period from April 27 to May 4 due to absorbing
624 and scattering solar radiation by aerosol. In contrast, LW radiation flux at the surface
625 of southern TP and IGP increased due to the positive radiative forcing of aerosol in the
626 atmosphere, with an increase of 4.1–4.6 Wm^{-2} in the southern TP from April 30 to May
627 1 (Figure 8e) and a large increase of 12.3–23.4 Wm^{-2} in the IGP from April 27 to May
628 4 (Figure 8g). Because of the aerosol's radiative cooling effects, the LH and SH fluxes
629 from the surface to the atmosphere in both regions decreased. Particularly, in the
630 southern TP, the LH and SH fluxes with the maximum decreases of 2.0 Wm^{-2} and 7.8
631 Wm^{-2} occurred on April 30 and April 29, respectively (Figure 8e). In the IGP, the LH
632 and SH fluxes, respectively, decreased by 4.1–7.4 Wm^{-2} and by 26.6–43.6 Wm^{-2} from
633 April 27 to May 4 (Figure 8g). The net energy flux at the surface decreased by 1.6–18.8

W m^{-2} in the southern TP (Figure 8e) and by 62.7–104.3 Wm^{-2} in the IGP (Figure 8g) from April 27 to May 4. Therefore, the energy arriving at the surface of southern TP and IGP decreased during this severe aerosol pollution event. For the diurnal change of surface energy, during 09:00–20:00 BJT in the southern TP, the SW, LH, SH, and net energy fluxes decreased by 7.8–19.9 Wm^{-2}, 0–2.4 Wm^{-2}, 4.7–12.2 Wm^{-2}, and 13.4–29 Wm^{-2}, respectively, while the LW flux increased by 0.3–2.9 Wm^{-2} (Figure 8f). During 09:00–20:00 BJT in the IGP, the SW, LH, SH, and net energy fluxes decreased by 46.1–144.2 Wm^{-2}, 7.5–16.6 Wm^{-2}, 9.6–100.1 Wm^{-2}, and 54.7–221.5 Wm^{-2} accordingly, whereas the LW flux increased by 8.5–30.5 Wm^{-2} (Figure 8h). Therefore, changes in surface energy mainly occur during the daytime.

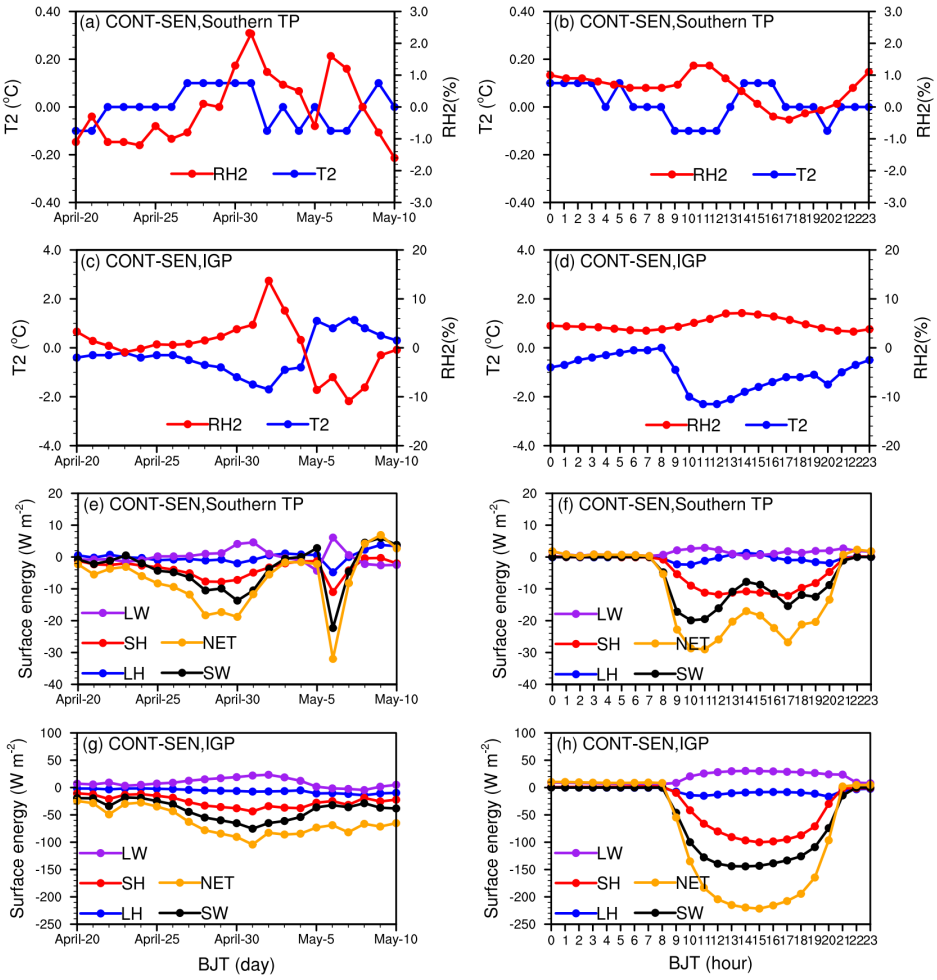

645 Figure 8. Time series of aerosol-induced daily changes in (a, c) meteorological variables
646 (T2 (°C), RH2 (%)) and (e, g) surface energy budget (SH, LH, LW radiation, SW
647 radiation, and net energy flux, Wm^{-2}) averaged for the (a, e) southern TP and (c, g) IGP
648 during the period from April 20 to May 10. Time series of aerosol-induced diurnal
649 changes in (b, d) meteorological variables and (f, h) surface energy budget averaged for
650 the period from April 27 to May 4, 2016 for the (b, f) southern TP and (d, h) IGP. LH
651 is latent heat, LW is long-wave radiation, SH is sensible heat, SW is shortwave radiation,
652 and NET is the sum of the total energy fluxes.
653
654 Figure 9 shows the spatial distribution of aerosol-induced changes in T2 and RH2
655 and aerosol radiative forcing (ARF) at the bottom of the atmosphere as well as in the
656 atmosphere, calculated by subtracting the model results of SEN from those of CONT
657 averaged during 09:00–20:00 BJT from April 27 to May 4. As seen in Figure 9a, the
658 aerosol-induced surface air temperature decreased over most parts of the study area
659 except for the TP, where surface air temperature increased, especially obvious in the
660 northern TP, with surface air temperature increasing by up to 1.0 °C. Because the TP is
661 one of the most pristine regions on the earth and has fewer human activities, there are
662 significantly less aerosols over the TP compared to the regions surrounding the TP.
663 Consequently, the surface-reaching solar radiation over the TP in the daytime is higher
664 than that of its surroundings, leading to higher surface temperature. A decrease in
665 surface-reaching solar radiation during daytime can lead to a decline in surface air
666 temperature. From Figure 9a, the largest surface air temperature decrease due to

667 aerosols occurred in South Asia since South Asia has large amounts of aerosols due to
668 rapid economic growth, industrialization, and unplanned urbanization compared to
669 other regions (Shi et al., 2020). The spatial distribution of aerosol-induced changes in
670 RH2 is opposite to that of T2, with increased RH2 appearing in most parts of the study
671 area and decreased RH2 on the TP. Specifically, the largest increase in RH2 occurred
672 in northern South Asia, since the aerosol-induced changes in water vapor mixing ratio
673 is very small, and the decrease in temperature can lead to a decrease in the saturation
674 pressure of water vapor and an increase in RH2 at the surface, which is beneficial for
675 the hygroscopic growth of aerosols (Gao et al., 2015). By analyzing the time–altitude
676 distribution of the diurnal cycle of aerosol impacts on temperature and relative humidity
677 (RH) averaged for the southern TP and IGP during the period from April 27 to May 4,
678 it is found that, consistent with the aerosol-induced changes in T2 and RH2, the aerosol-
679 induced changes in temperature and RH mainly occurred during daytime as well
680 (Figure S9). Specifically, in the southern TP, the maximum increase in temperature
681 with value up to 0.15 °C occurred in the middle troposphere (Figure S9a). However, in
682 the IGP, the temperature decreased near the surface with a maximum drop of more than
683 0.3 °C and increased in the middle troposphere with a maximum increase of more than
684 0.3 °C (Figure S9c). There is no doubt that such a temperature change increases the
685 stability of the atmosphere over both regions. Note that the temperature increase in the
686 middle troposphere over the southern TP is more significant than that in the IGP, which
687 is possibly correlated with the thermal pump role of the TP (Li and Yanai, 1996;Meehl,
688 1994;Yanai et al., 1992). The time–altitude distribution of the diurnal cycle of RH is

opposite to that of temperature, with RH increasing near the surface and decreasing in the middle troposphere (Figure S9b and Figure S9d). To be exact, RH decreased by 1.6% in the middle troposphere over the southern TP (Figure S9b), while in the IGP, RH increased near the surface with value greater than 3% and decreased by more than 3% in the middle troposphere (Figure S9d).

The ARF at the bottom of the atmosphere is negative over most parts of the study area except for the northern TP, where ARF is positive, with ARF up to 20 W m^{-2} (Figure 9c). The observed largest negative ARF occurred in northern South Asia and the Bay of Bengal, with values in a range of about −40–−120 Wm^{-2} (Figure 9c). Contrary to the spatial distribution of ARF at the bottom of the atmosphere, the ARF in the atmosphere is positive over most parts of the study area, with the largest ARF up to 110 Wm^{-2} in South Asia (Figure 9d). Thus, affected by aerosols, the atmospheric stratification over the study area is expected to be more stable.

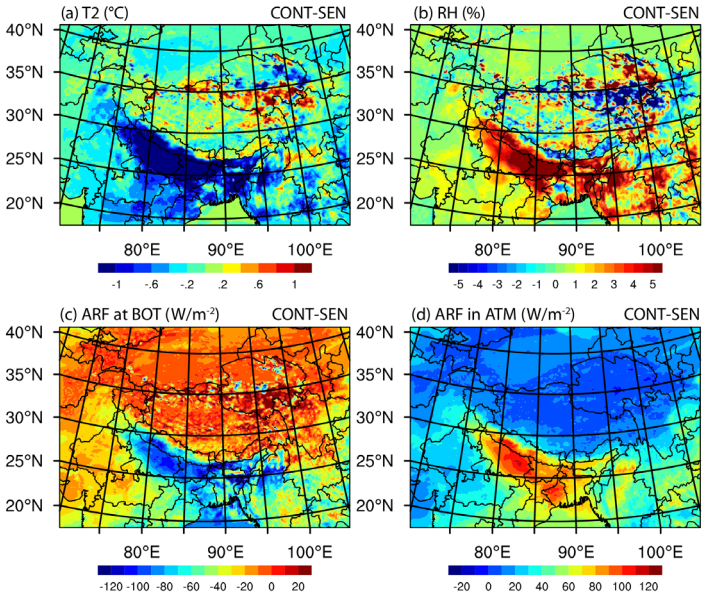

Figure 9. Spatial distribution of aerosol-induced changes in (a) T2 (°C) and (b) RH2 (%), and aerosol radiative forcing (ARF, Wm^{-2}) (c) at the bottom of (BOT) and (d) in

705 the atmosphere (ATM) averaged for 09:00–20:00 BJT during the period from April 27
706 to May 4, 2016.
707
708 From the above analysis, the aerosol-induced changes in meteorological
709 conditions and ARF have significant impact on atmospheric stability. The profile of
710 equivalent potential temperature (EPT) can be used to characterize the stability of the
711 atmosphere. Figure S10 in the SI shows the aerosol-induced changes in EPT profiles at
712 02:00, 08:00, 14:00, and 20:00 BJT averaged during the period from April 27 to May
713 4 in the southern TP and IGP. It can be seen that aerosol impact on EPT over the
714 southern TP with values in a range of about 0.08–0.24 K is overall smaller than that in
715 the IGP with values in a range of about −1.6–3.2 K because of low aerosol
716 concentrations in the southern TP and high aerosol concentrations in the IGP.
717 Specifically, at 08:00, 14:00, and 20:00 BJT, the EPT in the southern TP decreased with
718 height in the lower and middle troposphere, and increased with height above the middle
719 troposphere (Figure S10a). However, in the IGP, at 02:00 and 20:00 BJT, the EPT
720 decreased with height below 550 hPa and increased with height above 550 hPa; while
721 at 14:00 BJT, the EPT decreased with height below 650 hPa and increased with height
722 between 650 and 550 hPa (Figure S10b). Therefore, an obvious temperature inversion
723 was detected in the troposphere over the southern TP and IGP during the severe aerosol
724 pollution event.
725 Under a more stable atmosphere, the diurnal variation of surface BC concentration
726 from control experiment with aerosol-meteorology feedback and the aerosol-induced

changes in U10 and planetary boundary layer height (PBLH) over the southern TP and IGP are presented in Figure 10. Overall, the surface BC concentration over the southern TP and IGP was high during 20:00–08:00 BJT in the nighttime but low during 08:00–20:00 BJT in the daytime. Over the southern TP, the aerosol-induced PBLH decreased with value up to 55 m during 09:00–14:00 BJT and by 70 m during 18:00–20:00 BJT, while at other times of the day, no obvious change in PBLH was observed (Figure 10a). In the IGP, the aerosol-induced PBLH decreased during 10:00–20:00 BJT in the daytime, with the largest decrease of 1700 m occurring at 20:00 BJT (Figure 10b). Lower PBLH constrains the pollutants to diffuse in the vertical direction and is conducive to the accumulation of pollutants near the ground. The aerosol-induced U10 increased in the southern TP, with the maximum increase of 0.2 m/s appearing at 19:00 BJT (Figure 10a). In the IGP, the aerosol-induced U10 decreased, with the largest decrease of 0.7 m/s appearing at 20:00 BJT (Figure 10b). Therefore, aerosol induces significant changes in meteorological conditions in the southern TP and IGP during this severe aerosol pollution event.

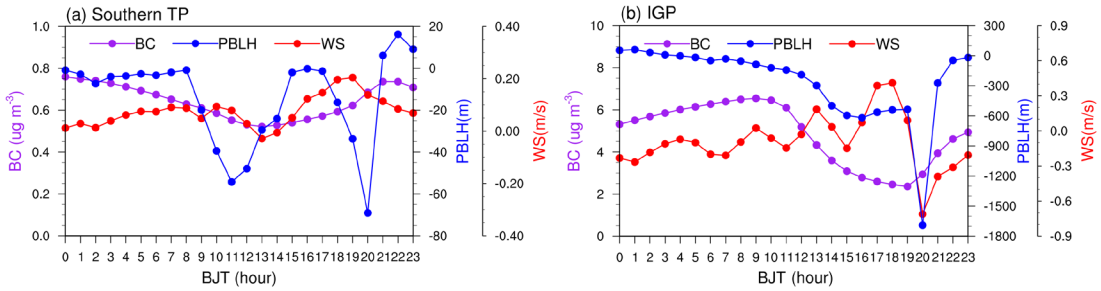

Figure 10. Diurnal variation of surface BC concentration (μg m^{-3}) from control experiment with aerosol-meteorology feedback (purple solid line) and aerosol-induced diurnal changes in 10-m wind speed (red solid line, WS, m s^{-1}) and PBLH (blue solid

line, m) averaged for (a) the southern TP and (b) IGP during the period from April 27 to May 4, 2016.

The aerosol-induced changes in meteorological conditions have important effect on surface BC concentration, which eventually exerts potential influence on aerosol pollution as well as weather and climate (Menon et al., 2002). Figure 11a and b show the hourly surface BC concentration from sensitive experiment without aerosol-meteorology feedback and the impact of aerosol-induced changes in meteorological variables on hourly surface BC concentration averaged over the southern TP and IGP during the period from April 20 to May 10. The corresponding diurnal cycle during the most polluted period from April 27 to May 4 are shown in Figure 11c and d. The change in percentage is calculated by comparing with the surface BC concentration from the experiment without aerosol-meteorology feedback. It can be seen that the aerosol-induced changes in meteorological conditions lead to a decrease of surface BC concentration with value up to 0.16 $\mu g/m^3$ (50%) in the southern TP. However, in the IGP, the aerosol-induced changes in meteorological conditions result in an increase in surface BC concentration with value up to 2.2 $\mu g/m^3$ (75%). Moreover, the higher the surface BC concentration is, the greater the variation in the surface BC concentration induced by meteorological conditions is. It should be noted that the time when the maximum decrease or increase in surface BC concentration occurs is not the time when the maximum surface BC concentration occurs. The diurnal changes in surface BC concentration during the most polluted period from April 27 to May 4 over the southern

768 TP indicate that the surface BC concentration is high during 20:00–07:00 BJT in the
769 nighttime and low during 08:00–19:00 BJT in the daytime, with the lowest
770 concentration of 0.6 μg/m^3 observed at 12:00 BJT. The changes in meteorological
771 conditions lead to a reduction of the surface BC concentration over the southern TP,
772 with the reduction primarily occurring during 11:00–19:00 BJT in the daytime and the
773 largest reduction of 0.06 μg/m^3 (12%) appearing at 15:00 BJT. The corresponding
774 diurnal changes in the IGP reveal that the surface BC concentration is high during
775 23:00–12:00 BJT and low during 13:00–22:00 BJT. The changes in the meteorological
776 conditions result in an increase in the surface BC concentration, with a relatively larger
777 increase of about 0.7–1.1 μg/m^3 occurring during 20:00–13:00 BJT. Therefore, the
778 changes in meteorological conditions enhance the diurnal variation of surface BC
779 concentration by decreasing the surface BC concentration in the southern TP and
780 increasing the surface BC concentration in the IGP.

781 Figure S11 in the SI shows the impact of aerosol-induced changes in
782 meteorological conditions on the spatial distribution of surface BC concentration
783 averaged during 09:00–20:00 BJT, April 27–May 4. Consistent with Figure 11, the
784 maximum increase in surface BC concentration induced by the changes in
785 meteorological conditions occurs in the IGP (northwestern South Asia), with values
786 greater than 1 μg/m^3. The corresponding surface BC concentration change in
787 percentage terms is also higher in northwestern South Asia with value up to 30%, and
788 is lower in the southeastern TP with value below 30% (Figure S11b). Taken together,
789 aerosols result in significant changes in meteorological conditions in the Southern TP

and IGP, with an obvious decrease in PBLH and U10 along with a more stable atmosphere in the IGP, and a decrease in PBLH but an increase in U10 accompanied by a stable atmosphere in the Southern TP. In addition, the aerosol-induced changes in meteorological conditions have substantial influence on surface aerosol concentration. For instance, in the IGP, the changes in meteorological conditions induced by aerosols are conducive to the accumulation of aerosols, thereby contributing to the formation of severe aerosol pollution event. Consequently, a positive feedback mechanism exists between aerosol concentration and aerosol-induced meteorological conditions in the IGP. However, as one of the major source regions of aerosols over the TP, the aerosol-induced changes in meteorological conditions in the IGP are not favorable for aerosols transporting to the southern TP.

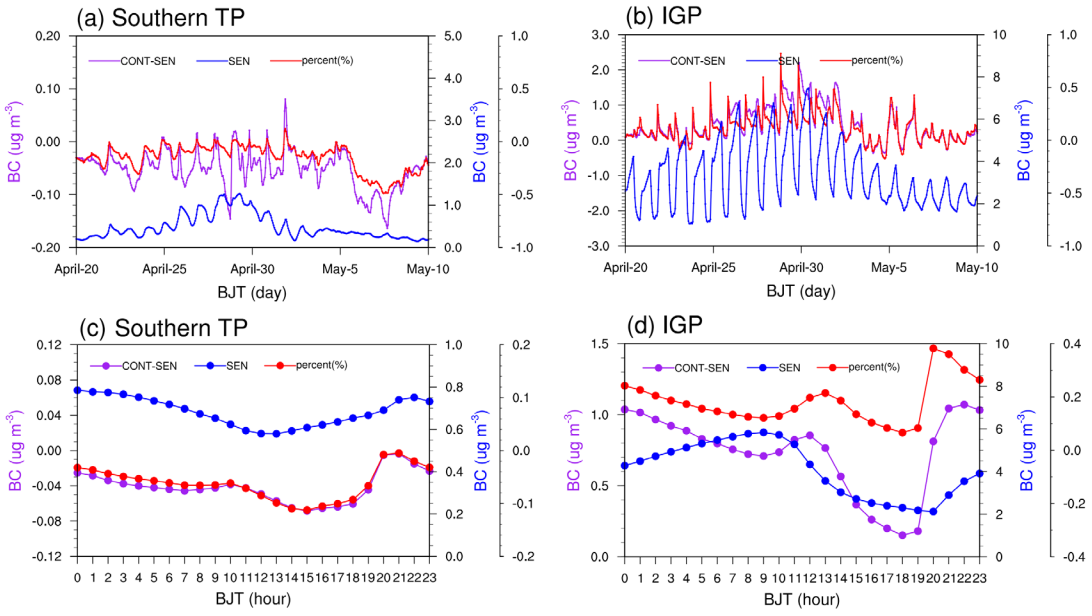

Figure 11. Time series of hourly surface BC concentration from SEN (blue solid line) averaged for (a) the southern TP and (b) the IGP during the period from April 20 to May 10, 2016 and the corresponding diurnal changes (blue solid line) averaged (c) for the

806 southern TP and (d) the IGP during the period from April 27 to May 4, 2016. The purple
807 solid line denotes the change value of surface BC concentration induced by
808 meteorological conditions. The red solid line indicates the corresponding change in
809 percentage terms compared to the surface BC concentration from the model results of
810 SEN.
811
812 *3.5 Impact of aerosol-meteorology feedback on the trans-boundary transport flux of*
813 *BC*
814 As discussed above, during the severe aerosol pollution event, northwestern South
815 Asia contributes more BC to the TP via cross-Himalayan transport and the largest BC
816 transport flux occurs at mountain valley in western Himalayas. Moreover, the aerosol-
817 meteorology feedback has substantial effect on surface BC concentration over the
818 southern TP and IGP. Yet what effect the aerosol-meteorology feedback having on the
819 trans-boundary transport flux of BC remains unclear, which deserves further
820 investigation. Therefore, this section is aimed at demonstrating the impact of aerosol-
821 meteorology feedback on the trans-boundary transport flux of BC during the severe
822 aerosol pollution event. Figure 12 shows the difference in longitude–height cross
823 section of BC transport flux along the cross line (shown as the blue dashed line in Figure
824 2) from the simulations with and without aerosol-meteorology feedback at 15:00 and
825 03:00 BJT averaged for the period from April 27 to May 4, 2016. It can be seen that,
826 during the daytime, in the central and western Himalayas (75–90 °E), the aerosol-
827 meteorology feedback overall increases the BC transport flux towards the TP at the

height of about 6–7 km but decreases the BC transport flux at the height of below 6 km; however, in the eastern Himalayas (90–98 °E), the aerosol-meteorology feedback decreases the BC transport flux exporting from the TP. During the nighttime, from 80 °E to 87 °E in the central Himalayas, the aerosol-meteorology feedback increases the BC transport flux towards the TP at the height of about 6–7 km but decreases the BC transport flux at the height of below 6 km; however, from 87 °E to 94 °E in the eastern Himalayas, the aerosol-meteorology feedback decreases the BC transport flux towards the TP at the height of below 7 km and from 94 °E to 98 °E, the aerosol-meteorology feedback decreases the BC transport flux exporting from the TP.

In addition, by analyzing the impact of aerosol-meteorology feedback on the BC transport flux at two typical mountain valley channels, it is found that, at valley-1, the feedback decreases the BC transport flux towards the TP during the daytime and nighttime; while at valley-2, the feedback decreases the BC transport flux towards the TP during the daytime and reduces the BC transport flux away from the TP during the nighttime. To better understand the effect of aerosol-meteorology feedback on the BC transport flux at two typical mountain valley channels of valley-1 and valley-2, we investigated the mean zonal and meridional wind speeds within 500 m above the ground level at both valleys during the daytime and nighttime from April 27 to May 4, 2016 (Table 2) from simulations with and without aerosol-meteorology feedback. It is found that, during the daytime, a westerly and a southerly prevail at valley-1 but an easterly and a southerly prevail at valley-2; during the night, an easterly and a northerly prevail at both valleys in both experiments. Specifically, at valley-1, the differences in zonal

and meridional wind speeds between the simulations with and without aerosol-meteorology feedback at 15:00 and 03:00 BJT averaged for the period from April 27 to May 4, 2016 show that, during the daytime, the aerosol-meteorology feedback overall decreases the westerly and southerly wind speeds, resulting in decreased BC transport flux towards the TP; during the night, the aerosol-meteorology feedback leads to increased easterly and northerly wind speeds, strengthening the BC transport flux being away from the TP. The corresponding results at valley-2 indicate that, during the daytime, the aerosol-meteorology feedback increases the easterly wind speed but decreases the southerly wind speed, resulting in decreased transport flux of BC towards the TP; during the night, the aerosol-meteorology feedback increases the easterly wind speed but decreases the northerly wind speed, leading to reduced BC transport flux away from the TP. It is to be emphasized that, at two typical mountain valley channels, the impact of aerosol-meteorology feedback on the BC transport flux averaged within 2000 m above the ground level (Table S3) are consistent with those averaged within 500 m above the ground level.

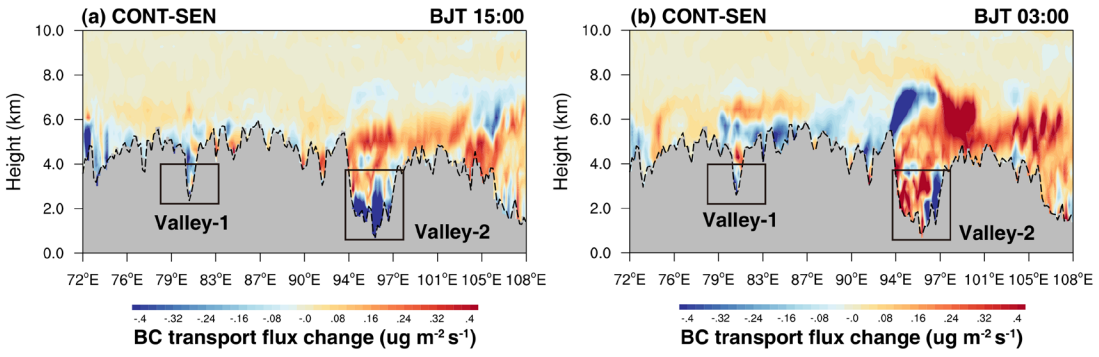

Figure 12. Difference in longitude–height cross section of BC transport flux along the cross line (shown as the blue dashed line in Figure 2) from the simulations with and without aerosol-meteorology feedback at 15:00 and 03:00 BJT averaged for the period

from April 27 to May 4, 2016. The difference in PBLH along the cross section is shown here as the black dashed line.

Table 2. The mean zonal and meridional wind speeds at two typical valley channels within 500 m above the ground level at 15:00 and 03:00 BJT averaged for the period from April 27 to May 4, 2016 between the CONT and SEN experiments. The differences in zonal and meridional wind speeds between the two experiments are also shown. Positive value denotes a westerly or a southerly and negative value denotes an easterly or a northerly.

500 m		15:00		03:00	
		Valley-1	Valley-2	Valley-1	Valley-2
CONT	U component	2.32	−1.90	−1.34	−1.19
	V component	4.74	1.35	−1.73	−1.56
SEN	U component	2.75	−1.43	−1.26	−1.07
	V component	4.94	1.61	−1.60	−1.92
CONT−SEN	U component	−0.43	−0.47	−0.08	−0.12
	V component	−0.2	−0.26	−0.13	0.36

Similarly, to analyze the impact of aerosol-meteorology feedback on the vertically integrated trans-boundary transport flux of BC, the difference in longitudinal distribution of integrated BC transport flux along the cross line shown as the blue dashed line in Figure 2 from the simulations with and without aerosol-meteorology feedback is shown in Figure 13. As can be seen, with the aerosol-meteorology feedback, the integrated BC transport flux from central and western Himalayas (to the west of 88 °E) to the TP overall decreases; however, in the eastern Himalayas, the aerosol-meteorology feedback reduces the integrated transport flux of BC away from the TP

887 (Figure 13). Therefore, the aerosol-meteorology feedback exerts substantial effect on
888 cross-Himalayan transport flux of BC.

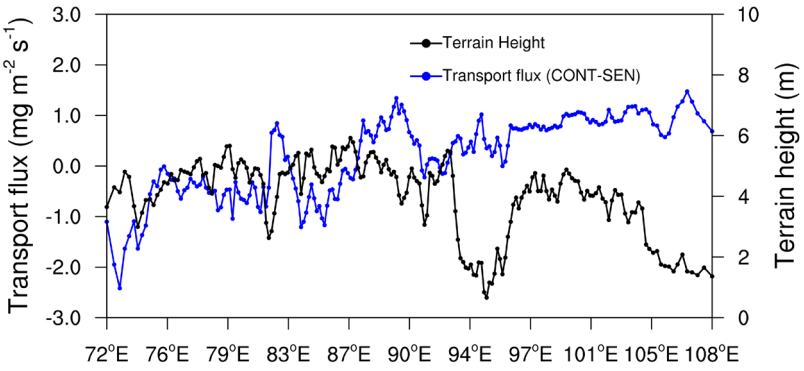

889

890 Figure 13. Difference in longitudinal distribution of vertically integrated BC transport
891 flux along the cross section in Figure 2 from simulations with and without aerosol-
892 meteorology feedback. The black line represents the terrain height.

893

894 # 4 Conclusion

895 The worst aerosol pollution episode ever recorded over the TP occurred during the
896 period from April 20 to May 10, 2016. The observed largest AOD at reference sites of
897 Nam Co and QOMS are 0.65 and 0.42, respectively. In this paper, the meteorological
898 causes of this severe aerosol pollution event, the BC transport flux, and the aerosol-
899 meteorology feedback as well as its effect on BC transport flux during this severe
900 aerosol pollution event are investigated by using observational and reanalysis datasets
901 and WRF-Chem simulation. By analyzing the evolution of weather maps at 500 hPa
902 over the study area during this severe aerosol pollution event, it is found that the plateau
903 vortex plays a critical role in increasing aerosol concentration in the inland of the TP.
904 However, in the southern TP, the increase in aerosol concentration could be attributed

to the long-range transport by southwesterly airflow in front of the trough.

With the acceptable performance of WRF-Chem model on simulating meteorological conditions and aerosols, we estimated the cross-Himalayan transport flux of BC. The results show that, in the central and western Himalayas, BC is imported into the TP during the day and night; however, in the eastern Himalayas, BC is imported into the TP during the day but exported slightly from the TP during the night; to the east of ~98 °E, BC is transported away from the TP during the day and night. The vertically integrated transport flux of BC along the cross line during the aerosol pollution event exhibits an overall decreasing trend from west to east, with the largest vertically integrated BC transport flux of 20.8 mg m^{-2} s^{-1} occurring at the deepest mountain valley in southwestern TP.

By designing experiments with or without aerosol-meteorology feedback, the feedback between aerosol and meteorology over the southern TP and IGP during this severe aerosol pollution event are investigated. It has been found that during the most polluted period from April 27 to May 4, aerosols lead to a slight change in surface air temperature in the southern TP but a significant decrease in surface air temperature with values in a range of 0.5–1.7 °C in the IGP. Vertically, in the southern TP, the largest temperature increase induced by aerosols occurs in the middle troposphere; however, in the IGP, aerosol-induced temperature decreases near the surface but increases in the middle troposphere. Spatially, the ARF is negative at the bottom of the atmosphere but is positive in the atmosphere. As a result, the atmospheric stratification over the study area is more stable. Additionally, affected by aerosols, U10 increases in the southern

TP, with the largest increase of 0.2 m/s appearing at 19:00 BJT; while in the IGP, U10 decreases, with the largest decrease of 0.7 m/s appearing at 20:00 BJT. In respect to PBLH, aerosols lead to a decrease by 55 m in PBLH during 09:00–14:00 BJT and by 60 m during 17:00–20:00 BJT in the southern TP; whereas in the IGP, a decrease in PBLH resulted from aerosols mainly occurs during 10:00–20:00 BJT in the daytime, with the largest decrease of 1300 m detected at 20:00 BJT. Therefore, aerosols exert an important effect on meteorological conditions. By contrast, the aerosol-induced changes in meteorological conditions can lead to a decrease of surface BC concentration with value up to 0.16 μg/m^3 (50%) in the southern TP and an increase of surface BC concentration with value up to 2.2 μg/m^3 (75%) in the IGP.

By investigating the impact of aerosol-meteorology feedback on the BC transport flux, it has been acquired that, with the aerosol-meteorology feedback, the vertically integrated transport flux of BC from central and western Himalayas to the TP overall decreases; however, in the eastern Himalayas, the aerosol-meteorology feedback reduces the vertically integrated transport flux of BC away from the TP. In particular, the corresponding results at two typical mountain valley channels in southwestern and southeastern TP reveal that the aerosol-meteorology feedback decreases the import of BC towards the TP at mountain valley channel in southwestern TP during the daytime and nighttime, while at mountain valley channel in the southeastern TP, the feedback decreases the import of BC towards the TP during the daytime and reduces the BC transport flux away from the TP during the nighttime.

Based on a severe aerosol pollution event, this study investigates the potential

impact of aerosol-meteorology feedback on the transport of BC to the southern TP for a relatively short period. Similar studies for a long-term period are necessary to examine whether the results obtained in this study are universal. In addition, a finer grid resolution of the model domain and an improvement in spatio-temporal resolution in emission inventory is needed to minimize the modeled biases caused by the TP's particularly complex topography. Furthermore, the results of this study show for the first time that the aerosol-meteorology feedback plays a substantial role in the transboundary transport of aerosols to the TP. Aerosols over the TP exert an important effect on the convective system over the TP (Zhao et al., 2020;Zhou et al., 2017). In the monsoon season, the convective activity is very vigorous over the TP. The transboundary transported aerosols along the slope from the foothill up to the TP via aerosol-meteorology feedback may also play a role. The potential impacts of aerosols on the regional climate over the TP using a high-resolution model that can resolve the complex topography of the TP deserve in-depth investigation.

Data Availability Statement

ERA-Interim reanalysis dataset is provided by European Centre for Medium-Range Weather Forecasts (https://www.ecmwf.int/en/forecasts/datasets/reanalysis-datasets/era-interim). The original simulation data used in this study are stored in a high-performance computing centre of Sun Yat-Sen University due to large data storage and can be made available from the corresponding author upon request. The ground-based AOD data are available through the AERONET website of

https://aeronet.gsfc.nasa.gov/. The satellite-based AOD are available through the website of https://ladsweb.modaps.eosdis.nasa.gov/archive/allData/61/MYD08_D3/. The National Centers for Environmental Prediction (NCEP) Final Analysis (FNL) data are available through the website of https://rda.ucar.edu/datasets/ds083.2/dataaccess/. The Emission Database for Global Atmospheric Research (EDGAR)-Hemispheric Transport Air Pollution version 2 (HTAPv2) emission inventory is available through the website of https://edgar.jrc.ec.europa.eu/dataset_htap_v2. The Fire INventory from NCAR (FINN) is available through the website of https://www.acom.ucar.edu/Data/fire/. CAM-Chem data are available through University Corporation for Atmospheric Research (https://www.acom.ucar.edu/cam-chem/cam-chem.shtml).

Author contributions

Shichang Kang and Haipeng Yu: Conceptualization, writing - review & editing. **Yuling Hu**: Visualization, validation, writing - original draft. **Shichang Kang**: Supervision. **Yuling Hu, Junhua Yang and Xintong Chen**: Methodology, software. **Xiufeng Yin and Pengfei Chen**: Data curation, validation.

Competing interests

The authors declare that they have no conflict of interest.

Acknowledgments

This study was supported by the National Natural Science Foundation of China (42205123), the Gansu Province Science Foundation for Youths (23JRRA617), the Chinese Academy of Sciences (XDA20040501). The authors would like to

993 acknowledge the National Centers for Environmental Prediction (NCEP) and the
994 European Centre for Medium-Range Weather Forecasts (ECMWF) for providing final
995 analysis data and reanalysis data, respectively. Finally, this work was supported by the
996 National Key Scientific and Technological Infrastructure project “Earth System
997 Numerical Simulation Facility” (EarthLab) and Supercomputing Center of Sun Yat-sen
998 University.

999 References

1000 Bharali, C., Nair, V. S., Chutia, L., and Babu, S. S.: Modeling of the Effects of Wintertime Aerosols on
1001 Boundary Layer Properties Over the Indo Gangetic Plain, *J. Geophys. Res.: Atmos.*, *124* (7), 4141-4157,
1002 https://doi.org/10.1029/2018jd029758, 2019.
1003 Bran, S. H., and Srivastava, R.: Investigation of PM2.5 mass concentration over India using a regional
1004 climate model, *Environ. Pollut.*, *224*, 484-493, https://doi.org/10.1016/j.envpol.2017.02.030, 2017.
1005 Buchard, V., Randles, C. A., da Silva, A. M., Darmenov, A., Colarco, P. R., Govindaraju, R., Ferrare, R., Hair,
1006 J., Beyersdorf, A. J., Ziemba, L. D., and Yu, H.: The MERRA-2 Aerosol Reanalysis, 1980 Onward. Part II:
1007 Evaluation and Case Studies, *J. Clim.*, *30* (17), 6851-6872, https://doi.org/10.1175/JCLI-D-16-0613.1,
1008 2017.
1009 Che, H., Gui, K., Xia, X., Wang, Y., Holben, B. N., Goloub, P., Cuevas-Agulló, E., Wang, H., Zheng, Y., Zhao,
1010 H., and Zhang, X.: Large contribution of meteorological factors to inter-decadal changes in regional
1011 aerosol optical depth, *Atmos. Chem. Phys.*, *19* (16), 10497-10523, https://doi.org/10.5194/acp-19-
1012 10497-2019, 2019.
1013 Chen, L., Zhu, J., Liao, H., Gao, Y., Qiu, Y. L., Zhang, M. G., Liu, Z. R., Li, N., and Wang, Y. S.: Assessing the
1014 formation and evolution mechanisms of severe haze pollution in the Beijing-Tianjin-Hebei region using
1015 process analysis, *Atmos. Chem. Phys.*, *19* (16), 10845-10864, https://doi.org/10.5194/acp-19-10845-
1016 2019, 2019a.
1017 Chen, X., Kang, S., Cong, Z., Yang, J., and Ma, Y.: Concentration, temporal variation, and sources of black
1018 carbon in the Mt. Everest region retrieved by real-time observation and simulation, *Atmos. Chem. Phys.*,
1019 *18* (17), 12859-12875, https://doi.org/10.5194/acp-18-12859-2018, 2018.
1020 Chen, Y., Yang, K., Zhou, D., Qin, J., and Guo, X.: Improving the Noah Land Surface Model in Arid Regions
1021 with an Appropriate Parameterization of the Thermal Roughness Length, *J. Hydrometeorol.*, *11* (4), 995-
1022 1006, https://doi.org/10.1175/2010JHM1185.1, 2010.
1023 Chen, Y., Zhou, Y., and Zhao, X.: PM2.5 over North China based on MODIS AOD and effect of
1024 meteorological elements during 2003–2015, *Front. Environ. Sci. Eng.*, *14* (2), 23,
1025 https://doi.org/10.1007/s11783-019-1202-8, 2019b.
1026 Chin, M., Ginoux, P., Kinne, S., Torres, O., Holben, B. N., Duncan, B. N., Martin, R. V., Logan, J. A., Higurashi,
1027 A., and Nakajima, T.: Tropospheric Aerosol Optical Thickness from the GOCART Model and Comparisons
1028 with Satellite and Sun Photometer Measurements, *J. Atmos. Sci.*, *59* (3), 461-483,
1029 https://doi.org/10.1175/1520-0469(2002)059<0461:TAOTFT>2.0.CO;2, 2002.

China, S., Scarnato, B., Owen, R. C., Zhang, B., Ampadu, M. T., Kumar, S., Dzepina, K., Dziobak, M. P., Fialho, P., Perlinger, J. A., Hueber, J., Helmig, D., Mazzoleni, L. R., and Mazzoleni, C.: Morphology and mixing state of aged soot particles at a remote marine free troposphere site: Implications for optical properties, *Geophys. Res. Lett.*, *42* (4), 1243-1250, https://doi.org/10.1002/2014GL062404, 2015.

Chung, C. E., Ramanathan, V., Kim, D., and Podgorny, I. A.: Global anthropogenic aerosol direct forcing derived from satellite and ground-based observations, *J. Geophys. Res.: Atmos.*, *110* (D24), https://doi.org/10.1029/2005JD006356, 2005.

Chung, C. E., Cha, H., Vihma, T., Räisänen, P., and Decremer, D.: On the possibilities to use atmospheric reanalyses to evaluate the warming structure in the Arctic, *Atmos. Chem. Phys.*, *13* (22), 11209-11219, https://doi.org/10.5194/acp-13-11209-2013, 2013.

Colarco, P., da Silva, A., Chin, M., and Diehl, T.: Online simulations of global aerosol distributions in the NASA GEOS-4 model and comparisons to satellite and ground-based aerosol optical depth, *J. Geophys. Res.: Atmos.*, *115* (D14), https://doi.org/10.1029/2009JD012820, 2010.

Duan, A., Wu, G., Zhang, Q., and Liu, Y.: New proofs of the recent climate warming over the Tibetan Plateau as a result of the increasing greenhouse gases emissions, *Chin. Sci. Bull.*, *51* (11), 1396-1400, https://doi.org/10.1007/s11434-006-1396-6, 2006.

Dubovik, O., and King, M. D.: A flexible inversion algorithm for retrieval of aerosol optical properties from Sun and sky radiance measurements, *J. Geophys. Res.: Atmos.*, *105* (D16), 20673-20696, https://doi.org/10.1029/2000JD900282, 2000.

Ek, M. B., Mitchell, K. E., Lin, Y., Rogers, E., Grunmann, P., Koren, V., Gayno, G., and Tarpley, J. D.: Implementation of Noah land surface model advances in the National Centers for Environmental Prediction operational mesoscale Eta model, *J. Geophys. Res.: Atmos.*, *108* (D22), 8851, https://doi.org/10.1029/2002JD003296, 2003.

Fast, J. D., Gustafson Jr, W. I., Easter, R. C., Zaveri, R. A., Barnard, J. C., Chapman, E. G., Grell, G. A., and Peckham, S. E.: Evolution of ozone, particulates, and aerosol direct radiative forcing in the vicinity of Houston using a fully coupled meteorology-chemistry-aerosol model, *J. Geophys. Res.: Atmos.*, *111* (D21), https://doi.org/10.1029/2005JD006721, 2006.

Flanner, M. G., Zender, C. S., Randerson, J. T., and Rasch, P. J.: Present-day climate forcing and response from black carbon in snow, *J. Geophys. Res.: Atmos.*, *112* (D11), https://doi.org/10.1029/2006JD008003, 2007.

Gao, M., Carmichael, G. R., Wang, Y., Saide, P. E., Yu, M., Xin, J., Liu, Z., and Wang, Z.: Modeling study of the 2010 regional haze event in the North China Plain, *Atmos. Chem. Phys.*, *16* (3), 1673-1691, https://doi.org/10.5194/acp-16-1673-2016, 2016.

Gao, Y., Zhang, M., Liu, Z., Wang, L., Wang, P., Xia, X., Tao, M., and Zhu, L.: Modeling the feedback between aerosol and meteorological variables in the atmospheric boundary layer during a severe fog–haze event over the North China Plain, *Atmos. Chem. Phys.*, *15* (8), 4279-4295, https://doi.org/10.5194/acp-15-4279-2015, 2015.

Gelaro, R., McCarty, W., Suárez, M. J., Todling, R., Molod, A., Takacs, L., Randles, C. A., Darmenov, A., Bosilovich, M. G., Reichle, R., Wargan, K., Coy, L., Cullather, R., Draper, C., Akella, S., Buchard, V., Conaty, A., da Silva, A. M., Gu, W., Kim, G.-K., Koster, R., Lucchesi, R., Merkova, D., Nielsen, J. E., Partyka, G., Pawson, S., Putman, W., Rienecker, M., Schubert, S. D., Sienkiewicz, M., and Zhao, B.: The Modern-Era Retrospective Analysis for Research and Applications, Version 2 (MERRA-2), *J. Clim.*, *30* (14), 5419-5454, https://doi.org/10.1175/JCLI-D-16-0758.1, 2017.

Grell, G. A., Peckham, S. E., Schmitz, R., McKeen, S. A., Frost, G., Skamarock, W. C., and Eder, B.: Fully

coupled “online” chemistry within the WRF model, *Atmos. Environ.*, *39* (37), 6957-6975, https://doi.org/10.1016/j.atmosenv.2005.04.027, 2005.
Grell, G. A., and Freitas, S. R.: A scale and aerosol aware stochastic convective parameterization for weather and air quality modeling, *Atmos. Chem. Phys.*, *14* (10), 5233-5250, https://doi.org/10.5194/acp-14-5233-2014, 2014.
Guenther, A., Karl, T., Harley, P., Wiedinmyer, C., Palmer, P. I., and Geron, C.: Estimates of global terrestrial isoprene emissions using MEGAN (Model of Emissions of Gases and Aerosols from Nature), *Atmos. Chem. Phys.*, *6* (11), 3181-3210, https://doi.org/10.5194/acp-6-3181-2006, 2006.
Guenther, A. B., Jiang, X., Heald, C. L., Sakulyanontvittaya, T., Duhl, T., Emmons, L. K., and Wang, X.: The Model of Emissions of Gases and Aerosols from Nature version 2.1 (MEGAN2.1): an extended and updated framework for modeling biogenic emissions, *Geosci. Model Dev.*, *5* (6), 1471-1492, https://doi.org/10.5194/gmd-5-1471-2012, 2012.
Hansen, J., and Nazarenko, L.: Soot climate forcing via snow and ice albedos, *PNAS*, *101* (2), 423, https://doi.org/10.1073/pnas.2237157100, 2004.
He, C., Liou, K. N., Takano, Y., Zhang, R., Levy Zamora, M., Yang, P., Li, Q., and Leung, L. R.: Variation of the radiative properties during black carbon aging: theoretical and experimental intercomparison, *Atmos. Chem. Phys.*, *15* (20), 11967-11980, https://doi.org/10.5194/acp-15-11967-2015, 2015.
Heidinger, A. K., Foster, M. J., Walther, A., and Zhao, X.: The Pathfinder Atmospheres–Extended AVHRR Climate Dataset, *Bull. Am. Meteorol. Soc.*, *95* (6), 909-922, https://doi.org/10.1175/BAMS-D-12-00246.1, 2014.
Holben, B. N., Eck, T. F., Slutsker, I., Tanré, D., Buis, J. P., Setzer, A., Vermote, E., Reagan, J. A., Kaufman, Y. J., Nakajima, T., Lavenu, F., Jankowiak, I., and Smirnov, A.: AERONET—A Federated Instrument Network and Data Archive for Aerosol Characterization, *Remote Sens. Environ.*, *66* (1), 1-16, https://doi.org/10.1016/S0034-4257(98)00031-5, 1998.
Hong, C. P., Zhang, Q., Zhang, Y., Davis, S. J., Zhang, X., Tong, D., Guan, D. B., Liu, Z., and He, K. B.: Weakening aerosol direct radiative effects mitigate climate penalty on Chinese air quality, *Nat. Clim. Change*, *10* (9), 845-850, https://doi.org/10.1038/s41558-020-0840-y, 2020.
Hsu, N. C., Jeong, M. J., Bettenhausen, C., Sayer, A. M., Hansell, R., Seftor, C. S., Huang, J., and Tsay, S. C.: Enhanced Deep Blue aerosol retrieval algorithm: The second generation, *J. Geophys. Res.: Atmos.*, *118* (16), 9296-9315, https://doi.org/10.1002/jgrd.50712, 2013.
Hu, Q., Liu, C., Li, Q., Liu, T., Ji, X., Zhu, Y., Xing, C., Liu, H., Tan, W., and Gao, M.: Vertical profiles of the transport fluxes of aerosol and its precursors between Beijing and its southwest cities, *Environ. Pollut.*, *312*, 119988, https://doi.org/10.1016/j.envpol.2022.119988, 2022a.
Hu, Y., Kang, S., Yang, J., Chen, X., Ji, Z., and Rai, M.: Transport of black carbon from Central and West Asia to the Tibetan Plateau: Seasonality and climate effect, *Atmos. Res.*, *267*, 105987, https://doi.org/10.1016/j.atmosres.2021.105987, 2022b.
Huang, X., Ding, A., Wang, Z., Ding, K., Gao, J., Chai, F., and Fu, C.: Amplified transboundary transport of haze by aerosol-boundary layer interaction in China, *Nat. Geosci.*, *13* (6), 428-+, https://doi.org/10.1038/s41561-020-0583-4, 2020.
Iacono, M. J., Delamere, J. S., Mlawer, E. J., Shephard, M. W., Clough, S. A., and Collins, W. D.: Radiative forcing by long-lived greenhouse gases: Calculations with the AER radiative transfer models, *J. Geophys. Res.: Atmos.*, *113* (D13), https://doi.org/10.1029/2008JD009944, 2008.
Janjić, Z. I.: The Step-Mountain Eta Coordinate Model: Further Developments of the Convection, Viscous Sublayer, and Turbulence Closure Schemes, *Mon. Weather Rev.*, *122* (5), 927-945,

https://doi.org/10.1175/1520-0493(1994)122<0927:TSMECM>2.0.CO;2, 1994.
Janssens-Maenhout, G., Crippa, M., Guizzardi, D., Dentener, F., Muntean, M., Pouliot, G., Keating, T., Zhang, Q., Kurokawa, J., Wankmüller, R., Denier van der Gon, H., Kuenen, J. J. P., Klimont, Z., Frost, G., Darras, S., Koffi, B., and Li, M.: HTAP_v2.2: a mosaic of regional and global emission grid maps for 2008 and 2010 to study hemispheric transport of air pollution, *Atmos. Chem. Phys.*, *15* (19), 11411-11432, https://doi.org/10.5194/acp-15-11411-2015, 2015.
Ji, Z., Kang, S., Zhang, D., Zhu, C., Wu, J., and Xu, Y.: Simulation of the anthropogenic aerosols over South Asia and their effects on Indian summer monsoon, *Clim. Dyn.*, *36* (9-10), 1633-1647, https://doi.org/10.1007/s00382-010-0982-0, 2011.
Kahn, R. A., Gaitley, B. J., Martonchik, J. V., Diner, D. J., Crean, K. A., and Holben, B.: Multiangle Imaging Spectroradiometer (MISR) global aerosol optical depth validation based on 2 years of coincident Aerosol Robotic Network (AERONET) observations, *J. Geophys. Res.: Atmos.*, *110* (D10), https://doi.org/10.1029/2004JD004706, 2005.
Kang, S., Xu, Y., You, Q., Flügel, W.-A., Pepin, N., and Yao, T.: Review of climate and cryospheric change in the Tibetan Plateau, *Environ. Res. Lett.*, *5* (1), 015101, https://doi.org/10.1088/1748-9326/5/1/015101, 2010.
Kang, S., Cong, Z., Wang, X., Zhang, Q., Ji, Z., Zhang, Y., and Xu, B.: The transboundary transport of air pollutants and their environmental impacts on Tibetan Plateau, *Chin. Sci. Bull.*, *64* (27), 2876-2884, 2019a.
Kang, S., Zhang, Q., Qian, Y., Ji, Z., Li, C., Cong, Z., Zhang, Y., Guo, J., Du, W., Huang, J., You, Q., Panday, A. K., Rupakheti, M., Chen, D., Gustafsson, Ö., Thiemens, M. H., and Qin, D.: Linking atmospheric pollution to cryospheric change in the Third Pole region: current progress and future prospects, *Natl. Sci. Rev.*, *6* (4), 796-809, https://doi.org/10.1093/nsr/nwz031, 2019b.
Lau, K. M., Kim, M. K., and Kim, K. M.: Asian summer monsoon anomalies induced by aerosol direct forcing: the role of the Tibetan Plateau, *Clim. Dyn.*, *26* (7), 855-864, https://doi.org/10.1007/s00382-006-0114-z, 2006.
Lelieveld, J., Crutzen, P. J., Ramanathan, V., Andreae, M. O., Brenninkmeijer, C. A. M., Campos, T., Cass, G. R., Dickerson, R. R., Fischer, H., de Gouw, J. A., Hansel, A., Jefferson, A., Kley, D., de Laat, A. T. J., Lal, S., Lawrence, M. G., Lobert, J. M., Mayol-Bracero, O., Mitra, A. P., Novakov, T., Oltmans, S. J., Prather, K. A., Reiner, T., Rodhe, H., Scheeren, H. A., Sikka, D., and Williams, J.: The Indian Ocean Experiment: Widespread Air Pollution from South and Southeast Asia, in: Paul J. Crutzen: A Pioneer on Atmospheric Chemistry and Climate Change in the Anthropocene, edited by: Crutzen, P. J., and Brauch, H. G., Springer International Publishing, Cham, 197-209, 2016.
Levy, R. C., Remer, L. A., Kleidman, R. G., Mattoo, S., Ichoku, C., Kahn, R., and Eck, T. F.: Global evaluation of the Collection 5 MODIS dark-target aerosol products over land, *Atmos. Chem. Phys.*, *10* (21), 10399-10420, https://doi.org/10.5194/acp-10-10399-2010, 2010.
Li, C., and Yanai, M.: The Onset and Interannual Variability of the Asian Summer Monsoon in Relation to Land–Sea Thermal Contrast, *J. Clim.*, *9* (2), 358-375, https://doi.org/10.1175/1520-0442(1996)009<0358:TOAIVO>2.0.CO;2, 1996.
Li, C., Bosch, C., Kang, S., Andersson, A., Chen, P., Zhang, Q., Cong, Z., Chen, B., Qin, D., and Gustafsson, Ö.: Sources of black carbon to the Himalayan–Tibetan Plateau glaciers, *Nat. Commun.*, *7* (1), 12574, https://doi.org/10.1038/ncomms12574, 2016a.
Li, J., Han, Z., Chen, L., Wu, Y., and Luo, L.: Modeling study of aerosol-meteorology feedback during winter haze events over the north China plain, *Atmos. Pollut. Res.*, *13* (2), 101311,

https://doi.org/10.1016/j.apr.2021.101311, 2022.
Li, J. W., Han, Z. W., Wu, Y. F., Xiong, Z., Xia, X. G., Li, J., Liang, L., and Zhang, R. J.: Aerosol radiative effects and feedbacks on boundary layer meteorology and PM(2.5)chemical components during winter haze events over the Beijing-Tianjin-Hebei region, *Atmos. Chem. Phys.*, *20* (14), 8659-8690, https://doi.org/10.5194/acp-20-8659-2020, 2020.
Li, Z., Lau, W. K. M., Ramanathan, V., Wu, G., Ding, Y., Manoj, M. G., Liu, J., Qian, Y., Li, J., Zhou, T., Fan, J., Rosenfeld, D., Ming, Y., Wang, Y., Huang, J., Wang, B., Xu, X., Lee, S. S., Cribb, M., Zhang, F., Yang, X., Zhao, C., Takemura, T., Wang, K., Xia, X., Yin, Y., Zhang, H., Guo, J., Zhai, P. M., Sugimoto, N., Babu, S. S., and Brasseur, G. P.: Aerosol and monsoon climate interactions over Asia, *Rev. Geophys.*, *54* (4), 866-929, https://doi.org/10.1002/2015RG000500, 2016b.
Liu, T., Gong, S., He, J., Yu, M., Wang, Q., Li, H., Liu, W., Zhang, J., Li, L., Wang, X., Li, S., Lu, Y., Du, H., Wang, Y., Zhou, C., Liu, H., and Zhao, Q.: Attributions of meteorological and emission factors to the 2015 winter severe haze pollution episodes in China's Jing-Jin-Ji area, *Atmos. Chem. Phys.*, *17* (4), 2971-2980, https://doi.org/10.5194/acp-17-2971-2017, 2017.
Liu, Y., Jia, R., Dai, T., Xie, Y., and Shi, G.: A review of aerosol optical properties and radiative effects, *J. Meteorolog. Res.*, *28* (6), 1003-1028, https://doi.org/10.1007/s13351-014-4045-z, 2014.
Meehl, G. A.: Coupled Land-Ocean-Atmosphere Processes and South Asian Monsoon Variability, *Science*, *266* (5183), 263-267, https://doi.org/10.1126/science.266.5183.263, 1994.
Menon, S., Hansen, J., Nazarenko, L., and Luo, Y.: Climate Effects of Black Carbon Aerosols in China and India, *Science*, *297* (5590), 2250-2253, https://doi.org/10.1126/science.1075159, 2002.
Morrison, H., Thompson, G., and Tatarskii, V.: Impact of Cloud Microphysics on the Development of Trailing Stratiform Precipitation in a Simulated Squall Line: Comparison of One- and Two-Moment Schemes, *Mon. Weather Rev.*, *137* (3), 991-1007, https://doi.org/10.1175/2008MWR2556.1, 2009.
O'Neill, N. T., Eck, T. F., Smirnov, A., Holben, B. N., and Thulasiraman, S.: Spectral discrimination of coarse and fine mode optical depth, *J. Geophys. Res.: Atmos.*, *108* (D17), https://doi.org/10.1029/2002JD002975, 2003.
O'Neill, N. T., Pancrati, O., Baibakov, K., Eloranta, E., Batchelor, R. L., Freemantle, J., McArthur, L. J. B., Strong, K., and Lindenmaier, R.: Occurrence of weak, sub-micron, tropospheric aerosol events at high Arctic latitudes, *Geophys. Res. Lett.*, *35* (14), https://doi.org/10.1029/2008GL033733, 2008.
Pokharel, M., Guang, J., Liu, B., Kang, S., Ma, Y., Holben, B., Xia, X. a., Xin, J., Ram, K., Rupakheti, D., Xin, W., Wu, G., Bhattarai, H., Zhao, C., and Cong, Z.: Aerosol Properties Over Tibetan Plateau From a Decade of AERONET Measurements: Baseline, Types, and Influencing Factors, *J. Geophys. Res.: Atmos.*, *124*, https://doi.org/10.1029/2019JD031293, 2019.
Qian, Y., Flanner, M. G., Leung, L. R., and Wang, W.: Sensitivity studies on the impacts of Tibetan Plateau snowpack pollution on the Asian hydrological cycle and monsoon climate, *Atmos. Chem. Phys.*, *11* (5), 1929-1948, https://doi.org/10.5194/acp-11-1929-2011, 2011.
Qin, Y., and Xie, S. D.: Spatial and temporal variation of anthropogenic black carbon emissions in China for the period 1980–2009, *Atmos. Chem. Phys.*, *12* (11), 4825-4841, https://doi.org/10.5194/acp-12-4825-2012, 2012.
Qiu, Y. L., Liao, H., Zhang, R. J., and Hu, J. L.: Simulated impacts of direct radiative effects of scattering and absorbing aerosols on surface layer aerosol concentrations in China during a heavily polluted event in February 2014, *J. Geophys. Res.: Atmos.*, *122* (11), 5955-5975, https://doi.org/10.1002/2016JD026309, 2017.
Rai, M., Kang, S., Yang, J., Chen, X., Hu, Y., and Rupakheti, D.: Tracing Atmospheric Anthropogenic Black

Carbon and Its Potential Radiative Response Over Pan-Third Pole Region: A Synoptic-Scale Analysis Using WRF-Chem, *J. Geophys. Res.: Atmos.*, *127* (6), e2021JD035772, https://doi.org/10.1029/2021JD035772, 2022.

Ramanathan, V., Chung, C., Kim, D., Bettge, T., Buja, L., Kiehl, J. T., Washington, W. M., Fu, Q., Sikka, D. R., and Wild, M.: Atmospheric brown clouds: Impacts on South Asian climate and hydrological cycle, *PNAS*, *102* (15), 5326, https://doi.org/10.1073/pnas.0500656102, 2005.

Ramanathan, V., and Carmichael, G.: Global and regional climate changes due to black carbon, *Nat. Geosci.*, *1* (4), 221-227, https://doi.org/10.1038/ngeo156, 2008.

Randles, C. A., da Silva, A. M., Buchard, V., Colarco, P. R., Darmenov, A., Govindaraju, R., Smirnov, A., Holben, B., Ferrare, R., Hair, J., Shinozuka, Y., and Flynn, C. J.: The MERRA-2 Aerosol Reanalysis, 1980 Onward. Part I: System Description and Data Assimilation Evaluation, *J. Clim.*, *30* (17), 6823-6850, https://doi.org/10.1175/JCLI-D-16-0609.1, 2017.

Shi, Y., Bilal, M., Ho, H. C., and Omar, A.: Urbanization and regional air pollution across South Asian developing countries – A nationwide land use regression for ambient PM2.5 assessment in Pakistan, *Environ. Pollut.*, *266*, 115145, https://doi.org/10.1016/j.envpol.2020.115145, 2020.

Skiles, S. M., Flanner, M., Cook, J. M., Dumont, M., and Painter, T. H.: Radiative forcing by light-absorbing particles in snow, *Nat. Clim. Change*, *8* (11), 964-971, https://doi.org/10.1038/s41558-018-0296-5, 2018.

Smirnov, A., Holben, B. N., Slutsker, I., Giles, D. M., McClain, C. R., Eck, T. F., Sakerin, S. M., Macke, A., Croot, P., Zibordi, G., Quinn, P. K., Sciare, J., Kinne, S., Harvey, M., Smyth, T. J., Piketh, S., Zielinski, T., Proshutinsky, A., Goes, J. I., Nelson, N. B., Larouche, P., Radionov, V. F., Goloub, P., Krishna Moorthy, K., Matarrese, R., Robertson, E. J., and Jourdin, F.: Maritime Aerosol Network as a component of Aerosol Robotic Network, *J. Geophys. Res.: Atmos.*, *114* (D6), https://doi.org/10.1029/2008JD011257, 2009.

Srivastava, P., and Sharan, M.: An Analytical Formulation of the Monin–Obukhov Stability Parameter in the Atmospheric Surface Layer Under Unstable Conditions, *Boundary Layer Meteorol.*, *165* (2), 371-384, https://doi.org/10.1007/s10546-017-0273-y, 2017.

Sun, E., Xu, X., Che, H., Tang, Z., Gui, K., An, L., Lu, C., and Shi, G.: Variation in MERRA-2 aerosol optical depth and absorption aerosol optical depth over China from 1980 to 2017, *J. Atmos. Sol. Terr. Phys.*, *186*, 8-19, https://doi.org/10.1016/j.jastp.2019.01.019, 2019.

Wang, P., Guo, H., Hu, J., Kota, S. H., Ying, Q., and Zhang, H.: Responses of PM2.5 and O3 concentrations to changes of meteorology and emissions in China, *Sci. Total Environ.*, *662*, 297-306, https://doi.org/10.1016/j.scitotenv.2019.01.227, 2019.

Wiedinmyer, C., Akagi, S. K., Yokelson, R. J., Emmons, L. K., Al-Saadi, J. A., Orlando, J. J., and Soja, A. J.: The Fire INventory from NCAR (FINN): a high resolution global model to estimate the emissions from open burning, *Geosci. Model Dev.*, *4* (3), 625-641, https://doi.org/10.5194/gmd-4-625-2011, 2011.

Wu, G., Liu, Y., Zhang, Q., Duan, A., Wang, T., Wan, R., Liu, X., Li, W., Wang, Z., and Liang, X.: The Influence of Mechanical and Thermal Forcing by the Tibetan Plateau on Asian Climate, *J. Hydrometeorol.*, *8* (4), 770-789, https://doi.org/10.1175/JHM609.1, 2007.

Wu, J., Fu, C., Xu, Y., Tang, J. P., Wang, W., and Wang, Z.: Simulation of direct effects of black carbon aerosol on temperature and hydrological cycle in Asia by a Regional Climate Model, *Meteorol. Atmos. Phys.*, *100* (1), 179-193, https://doi.org/10.1007/s00703-008-0302-y, 2008.

Wu, J. R., Bei, N. F., Hu, B., Liu, S. X., Zhou, M., Wang, Q. Y., Li, X., Liu, L., Feng, T., Liu, Z. R., Wang, Y. C., Cao, J. J., Tie, X. X., Wang, J., Molina, L. T., and Li, G. H.: Aerosol-radiation feedback deteriorates the wintertime haze in the North China Plain, *Atmos. Chem. Phys.*, *19* (13), 8703-8719, https://doi.org/10.5194/acp-19-8703-2019, 2019.

Xu, B., Cao, J., Hansen, J., Yao, T., Joswia, D. R., Wang, N., Wu, G., Wang, M., Zhao, H., Yang, W., Liu, X., and He, J.: Black soot and the survival of Tibetan glaciers, *PNAS*, *106* (52), 22114, https://doi.org/10.1073/pnas.0910444106, 2009.

Yanai, M., Li, C., and Song, Z.: Seasonal Heating of the Tibetan Plateau and Its Effects on the Evolution of the Asian Summer Monsoon, *Journal of the Meteorological Society of Japan. Ser. II*, *70* (1B), 319-351, https://doi.org/10.2151/jmsj1965.70.1B_319, 1992.

Yang, J., Kang, S., Ji, Z., and Chen, D.: Modeling the origin of anthropogenic black carbon and its climatic effect over the Tibetan Plateau and surrounding regions, *J. Geophys. Res.: Atmos.*, *123* (2), 671-692, https://doi.org/10.1002/2017JD027282, 2018.

Yao, T., Pu, J., Lu, A., Wang, Y., and Yu, W.: Recent Glacial Retreat and Its Impact on Hydrological Processes on the Tibetan Plateau, China, and Surrounding Regions, *Arctic, Antarctic, and Alpine Research*, *39* (4), 642-650, https://doi.org/10.1657/1523-0430(07-510)[YAO]2.0.CO;2, 2007.

Yao, T., Bolch, T., Chen, D., Gao, J., Immerzeel, W., Piao, S., Su, F., Thompson, L., Wada, Y., Wang, L., Wang, T., Wu, G., Xu, B., Yang, W., Zhang, G., and Zhao, P.: The imbalance of the Asian water tower, *Nat. Rev. Earth Env.*, https://doi.org/10.1038/s43017-022-00299-4, 2022.

You, Q., Min, J., and Kang, S.: Rapid warming in the Tibetan Plateau from observations and CMIP5 models in recent decades, *Int. J. Climatol.*, *36* (6), 2660-2670, https://doi.org/10.1002/joc.4520, 2016.

You, Q., Cai, Z., Pepin, N., Chen, D., Ahrens, B., Jiang, Z., Wu, F., Kang, S., Zhang, R., Wu, T., Wang, P., Li, M., Zuo, Z., Gao, Y., Zhai, P., and Zhang, Y.: Warming amplification over the Arctic Pole and Third Pole: Trends, mechanisms and consequences, *Earth Sci. Rev.*, *217*, 103625, https://doi.org/10.1016/j.earscirev.2021.103625, 2021.

Zaveri, R. A., and Peters, L. K.: A new lumped structure photochemical mechanism for large-scale applications, *J. Geophys. Res.: Atmos.*, *104* (D23), 30387-30415, https://doi.org/10.1029/1999JD900876, 1999.

Zaveri, R. A., Easter, R. C., Fast, J. D., and Peters, L. K.: Model for Simulating Aerosol Interactions and Chemistry (MOSAIC), *J. Geophys. Res.*, *113* (D13), https://doi.org/10.1029/2007jd008782, 2008.

Zhang, M., Zhao, C., Cong, Z., Du, Q., Xu, M., Chen, Y., Chen, M., Li, R., Fu, Y., Zhong, L., Kang, S., Zhao, D., and Yang, Y.: Impact of topography on black carbon transport to the southern Tibetan Plateau during the pre-monsoon season and its climatic implication, *Atmos. Chem. Phys.*, *20* (10), 5923-5943, https://doi.org/10.5194/acp-20-5923-2020, 2020.

Zhang, X., Zhang, Q., Hong, C., Zheng, Y., Geng, G., Tong, D., Zhang, Y., and Zhang, X.: Enhancement of PM2.5 Concentrations by Aerosol-Meteorology Interactions Over China, *J. Geophys. Res.: Atmos.*, *123* (2), 1179-1194, https://doi.org/10.1002/2017JD027524, 2018a.

Zhang, X., Xu, X., Ding, Y., Liu, Y., Zhang, H., Wang, Y., and Zhong, J.: The impact of meteorological changes from 2013 to 2017 on PM2.5 mass reduction in key regions in China, *Science China Earth Sciences*, *62* (12), 1885-1902, https://doi.org/10.1007/s11430-019-9343-3, 2019.

Zhang, X. Y., Zhong, J. T., Wang, J. Z., Wang, Y. Q., and Liu, Y. J.: The interdecadal worsening of weather conditions affecting aerosol pollution in the Beijing area in relation to climate warming, *Atmos. Chem. Phys.*, *18* (8), 5991-5999, https://doi.org/10.5194/acp-18-5991-2018, 2018b.

Zhang, Y., Gao, T., Kang, S., Shangguan, D., and Luo, X.: Albedo reduction as an important driver for glacier melting in Tibetan Plateau and its surrounding areas, *Earth Sci. Rev.*, *220*, 103735, https://doi.org/10.1016/j.earscirev.2021.103735, 2021.

Zhao, B., Liou, K. N., Gu, Y., Li, Q. B., Jiang, J. H., Su, H., He, C. L., Tseng, H. L. R., Wang, S. X., Liu, R., Qi, L., Lee, W. L., and Hao, J. M.: Enhanced PM2.5 pollution in China due to aerosol-cloud interactions, *Sci.*

Rep., *7*, https://doi.org/10.1038/s41598-017-04096-8, 2017.

Zhao, C., Yang, Y., Fan, H., Huang, J., Fu, Y., Zhang, X., Kang, S., Cong, Z., Letu, H., and Menenti, M.: Aerosol characteristics and impacts on weather and climate over the Tibetan Plateau, *Natl. Sci. Rev.*, *7* (3), 492-495, https://doi.org/10.1093/nsr/nwz184, 2020.

Zheng, B., Zhang, Q., Zhang, Y., He, K. B., Wang, K., Zheng, G. J., Duan, F. K., Ma, Y. L., and Kimoto, T.: Heterogeneous chemistry: a mechanism missing in current models to explain secondary inorganic aerosol formation during the January 2013 haze episode in North China, *Atmos. Chem. Phys.*, *15* (4), 2031-2049, https://doi.org/10.5194/acp-15-2031-2015, 2015.

Zhong, J. T., Zhang, X. Y., Dong, Y. S., Wang, Y. Q., Liu, C., Wang, J. Z., Zhang, Y. M., and Che, H. C.: Feedback effects of boundary-layer meteorological factors on cumulative explosive growth of PM2.5 during winter heavy pollution episodes in Beijing from 2013 to 2016, *Atmos. Chem. Phys.*, *18* (1), 247-258, https://doi.org/10.5194/acp-18-247-2018, 2018.

Zhou, X., Bei, N., Liu, H., Cao, J., Xing, L., Lei, W., Molina, L. T., and Li, G.: Aerosol effects on the development of cumulus clouds over the Tibetan Plateau, *Atmos. Chem. Phys.*, *17* (12), 7423-7434, https://doi.org/10.5194/acp-17-7423-2017, 2017.